Title: A Novel Human Extravascular Monocyte Subset with Antiviral Functions Is Crucial for Resolving Lung Tissue Infection

Short Title: Extravascular Monocytes Resolve Lung Infection

One sentence summary: We identified a novel human subset of lung extravascular monocytes with antiviral functions that play a critical role in resolving SARS-CoV-2 infection from human lung tissues in an immunologically naïve context.

Devin Kenney[1,2], Aoife K. O'Connell[1,2,4], Anna E. Tseng[1,2,4], Jacquelyn Turcinovic[1,2,3], Maegan L. Sheehan[7,12], Adam D. Nitido[7,12], Paige Montanaro[2,4], Hans P. Gertje[2,4], Maria Ericsson[6], John H. Connor[1,2], Vladimir Vrbanac[7], Nicholas A. Crossland[1,2,4], Christelle Harly[8,9,12]*, Alejandro B. Balazs[7,12]*, and Florian Douam[1,2,12,13] *

[1]Department of Virology, Immunology, and Microbiology, Boston University Chobanian & Avedisian School of Medicine, Boston, MA, USA.

[2] National Emerging Infectious Diseases Laboratories, Boston University, Boston, MA, USA.

[3] Bioinformatics Program, Boston University, Boston, MA, USA.

[4] Department of Pathology and Laboratory Medicine, Boston University Chobanian & Avedisian School of Medicine, Boston, MA, USA.

[6] Electron Microscopy Core Facility, Harvard Medical School, Boston, MA, USA.

[7] Ragon Institute of MGH, MIT and Harvard, Cambridge, MA, USA.

[8] Université de Nantes, INSERM, CNRS, CRCINA, Nantes, France

[9] LabEx IGO 'Immunotherapy, Graft, Oncology', Nantes, France.

[12] These authors contributed equally to the work.

[13] Lead contact

*Correspondence:

Florian Douam, National Emerging Infectious Diseases Laboratories, 620 Albany Street Boston MA 02118 USA, +1-617-358-9174, fdouam@bu.edu.

Alejandro B. Balazs, Ragon Institute of MGH Harvard and MIT, 400 Technology Square Cambridge MA 02139 USA, +1-857-268-7197, abalazs@mgh.harvard.edu.

Christelle Harly, CRCINA - Institut de Recherche en Santé de Nantes Université, 8 quai Moncousu 44 007 Nantes France, +33-2 28 08 02 08, christelle.harly@inserm.fr.

The authors have declared that no conflict of interest exists.

ABSTRACT

The recurring emergence of novel respiratory viruses has highlighted our poor understanding of the human immune mechanisms governing the resolution of lung infection in an immunologically naïve context. Using SARS-CoV-2 as a prototypical emerging respiratory virus, we leveraged mice co-engrafted with a genetically matched fetal lung xenograft (fLX) and a human immune system (BLT-L mice) to investigate such mechanisms. While BLT-L mice effectively resolve SARS-CoV-2 infection following acute viral replication in fLX, viral clearance is robustly abrogated through systemic depletion of CD4+, but not CD3+ or CD8+ cells, resulting in persistent infection. Leveraging single-cell transcriptomics to uncover the CD4-expressing subsets driving infection resolution, we identified a novel subset of lung extravascular inflammatory monocytes (ExiMO) with antiviral functions. ExiMO are the dominant CD163-expressing myeloid population emerging in fLX upon acute infection and derive from recruited circulating CD4+ monocytes. They are highly enriched in viral RNA and elicit a robust antiviral response before vanishing from tissues when infection resolves. Notably, systemic CD4+ cell depletion results in impaired recruitment of CD163+ cells into fLX and leads to a state of immune tolerance and chronic infection defined by the absence of ExiMO antiviral responses. Together, our study uncovers ExiMO as major sentinels driving SARS-CoV-2 infection resolution in human lung tissues without pre-existing immunity. This work expands our understanding of lung extravascular monocytes and unravels novel facets of the cellular determinants governing our vulnerability to viral respiratory pathogens.

INTRODUCTION

Human emerging respiratory viruses (hERVs), including MERS-CoV, new influenza A strains, and more recently, SARS-CoV-2, the etiologic agent of COVID-19, have reignited the need to understand immunological mechanisms that can protect us against these pathogens when no pre-existing and/or cross-reactivity immunity exists. While these non-experienced immune mechanisms harbor a pivotal role in our inherent resistance against antigenically novel hERVs and their disruptive impact on public health, the scarcity of experimental systems that recapitulate lung-resident human immune responses has made their investigation challenging.

Human studies are associated with logistical and experimental challenges, such as the need to capture early pulmonary immune responses in infected individuals and/or in the validation of purely correlative findings. While these challenges can be overcome through experimental human infection studies, longitudinal lung-resident immune responses in infected volunteers remain hardly accessible. Notably, a recent human challenge study uncovered novel immunological signatures of protection from SARS-CoV-2 in humans (*1*). However, sample analysis was limited to peripheral blood and nasopharyngeal swabs, concealing major tissue-resident immunological processes associated with protection, such as extravasation of recruited immune lineages and their differentiation process to combat and resolve infection.

In contrast, large and small animal models have been developed to support infection with hERVs. However, the high cost and limited reagent availability associated with non-human primate models and the large divergence between rodent and human immune systems underscore the need for additional models capable of recapitulating human protective immune responses to HERVs in an immunologically non-experienced context.

Mice co-engrafted with human fetal lung xenograft (fLX) and a human immune system (HIS) have been reported to support infection by multiple hERVs, including human cytomegalovirus (HCMV), Middle East respiratory syndrome coronavirus (MERS-CoV) and SARS-CoV-2 (*2-4*), and mount lung-resident human immune responses against these pathogens.

105 Recently, our group reported that mice engrafted with fLX are highly susceptible to SARS-CoV-2
106 infection and lung tissue damage and support persistent viral infection. However, co-engraftment
107 of these animals with fLX and a HIS in a xenorecipient strain supporting enhanced myelopoiesis
108 (i.e., HNFL mouse model) prevented any detectable viral replication in fLX, resulting in complete
109 lung tissue protection from histopathology (*3*). Our findings unraveled a human macrophage
110 antiviral signature as a correlate of non-experienced immunity against SARS-CoV-2 infection.
111 However, the non-experienced immune mechanisms governing the resolution of SARS-CoV-2
112 infection in the context of extensive viral replication in lung tissues, which more likely describes
113 mild cases of COVID-19, have remained elusive. This study, which uses SARS-CoV-2 as a
114 prototypical hERV, aims to unravel some of these mechanisms.

115 Unlike the HNFL mouse model, immunodeficient mice co-engrafted with fLX and a
116 genetically matched human immune system, fetal liver, and thymus (BLT-L mice) support acute
117 SARS-CoV-2 infection, consistent with previous reports (*2, 4*). However, the infection quickly
118 resolves following a viral replication peak at 2 days post-inoculation (dpi), making this model
119 suitable for examining mechanisms of non-experienced antiviral immunity in the context of HERV
120 infection of lung tissues. Notably, systemic depletion of CD4+ cells, but not CD3+ T-cells or CD8+
121 cells, robustly abrogates infection resolution and results in persistent viral replication in fLX of
122 BLT-L mice. Using single-cell transcriptomic and multiplexed immunohistochemistry (mIHC)
123 approaches, we uncovered a novel subset of lung extravascular inflammatory monocytes
124 (ExiMO). ExiMO are directly related to intravascular CD4+ patrolling monocytes recruited into fLX
125 during acute infection, and are the dominant CD163-expressing myeloid subset to emerge in fLX
126 upon acute infection. They are highly enriched in viral RNA and elicit a uniquely robust antiviral
127 response. In accordance with our depletion findings, CD4+ cell depletion reduces CD163+
128 recruitment into fLX and promotes a state of immune tolerance characterized by the absence of
129 major antiviral cytokines expressed by ExiMO. CD4+ cell depletion also induces systemic and
130 lung signatures of chronic infection, underlining how ExiMO are critical to avert long-lasting viral

131 persistence. Collectively, our work sheds light on a novel cellular mediator driving naïve immunity
132 against SARS-CoV-2 in human lung tissues. To our knowledge, our study is the first to uncover
133 lung extravascular monocytes with antiviral functions and contributes to enhancing our
134 understanding of the cellular determinants defining human susceptibility to hERVs.
135

136 **RESULTS**

137 **BLT-L mice effectively clear SARS-CoV-2 infection following acute viral replication**

138 Previous work from our laboratory (*3*) and others (*2, 4, 5*) have shown that
139 immunodeficient mice can successfully be engrafted with human fetal lung xenograft (fLX) alone
140 or in combination with a human immune system (HIS). In this study, we leveraged a previously
141 reported mouse model co-engrafted with fetal liver and thymus as well as with human
142 hematopoietic stem cells (HSC) and fLX (BLT-L mice) (*5*). Fetal liver and thymus were engrafted
143 under the renal capsule of adult NOD.Cg-*Prkdc*^{scid} *Il2rg*^{tm1Wjl}/SzJ (NSG) mice (12-16 weeks old)
144 prior to intravenous HSC injection. A piece of fetal lung tissue was subcutaneously engrafted on
145 the flank of each animal, as described previously (*5*). To determine the susceptibility of BLT-L
146 mice to SARS-CoV-2 infection and their ability to effectively clear infection, BLT-L mice were
147 inoculated with SARS-CoV-2 (2019-nCoV/USA_WA1/2020) via intra-graft injection. We used a
148 viral dose (10^6 PFU) that we previously established to drive robust and persistent infection in fLX
149 of immunodeficient mice not engrafted with an HIS (*3*).

150 Throughout the course of infection, mice did not display any weight loss (**Fig. 1A)** or
151 clinical signs of disease such as lethargy or lack of responsiveness (data not shown). To assess
152 lung histopathology and viral titers longitudinally, fLX were collected at 2, 6, and 12 dpi.
153 Immunohistochemistry (IHC) for SARS-CoV-2 Spike (S) protein revealed infection of alveolar
154 epithelium in fLX at 2 dpi, while the majority of viral antigen was cleared by 6 dpi and became
155 undetectable by 12 dpi (**Fig.1B**$^{a\text{-}d}$). SARS-CoV-2 S was primarily detected in the cytoplasm of
156 alveolar epithelium morphologically consistent with type II pneumocytes (AT2 cells) and

157 macrophages within alveolar spaces admixed with necrotic cellular debris and bronchiole
158 epithelium, consistent with the primary cell targets of SARS-CoV-2 (**Fig.1B[b]**). These findings were
159 independently confirmed through IHC for SARS-CoV-2 nucleoprotein N (**Fig. S1A-D**).
160 Transmission electron microscopy (TEM) imaging of fLX at 2 dpi substantiated evidence of
161 productive fLX infection, as indicated by the presence of viral particles in the cytosol of epithelial
162 cells and budding/invagination of virions (**Fig. S1E-G**). Viral titer quantification in fLX also
163 supported evidence of acute infection at 2 dpi prior to effective resolution (**Fig.1C**). A significant
164 amount of infectious viral particles could be recovered from fLX at 2 dpi (3.20 ± 2.52 log([PFU/mg
165 of tissue]), but not at 6 dpi (0.281 ± 0.688 log[PFU/mg of tissue]) and 12 dpi (0.111 ± 0.293
166 log[PFU/mg of tissue]) (**Fig. 1C**).

167 Next, we examined histopathological phenotypes associated with active and resolved
168 infection. Interpretation of hematoxylin and eosin (H&E) staining illustrated denuding of
169 pneumocytes, neutrophil infiltration, edema, hemorrhage, thrombosis, and pneumocyte necrosis,
170 which correlated with sites of infection at 2 dpi (**Fig. 1B[e,f] and Fig. S1H-J**). No major disease
171 phenotypes were observed at 6 and 12 dpi compared to naïve fLX, underscoring that fLX can
172 mount repair mechanisms upon resolution of infection (**Fig. 1B[g,h]**). A previously described semi-
173 quantitative histopathological scoring system (*3*) provided statistical confirmation for a significant
174 increase in lung pathology at 2 dpi, which was no longer apparent at 6 dpi (**Fig. 1D**) or 12 dpi. Of
175 note, minor lung pathology was observed at baseline (naïve), likely reflecting limited graft vs. host
176 disease. Together, BLT-L fLX recapitulates important hallmarks of acute SARS-CoV-2 infection,
177 including viral replication and histopathological manifestations of disease, prior to effective viral
178 clearance and lung tissue repair.

179

180 **Humoral responses do not drive SARS-CoV-2 clearance in BLT-L mice despite evidence of**
181 **Spike selective pressure.**

182 We first asked whether SARS-CoV-2 infection resolution was driven by human
183 neutralizing humoral responses. No neutralization against infectious SARS-CoV-2 was detected
184 from the serum of BLT-L mice collected at 2 or 12 dpi (**Fig. S1K,L**). This is consistent with the
185 rapid clearance of infectious viral particles by 6 dpi, and the known caveat that humanized mice
186 mount limited humoral responses (*6*). However, viral genome sequencing from acutely infected
187 fLX showed that 75% of 2 dpi-associated viral sequences exhibited the selection of two stable
188 mutations not observed in our inoculum and located in the Spike N-terminal domain (NTD): an
189 insertion (216KLRS) and a non-synonymous mutation (R245H) (**Fig. S1M,N Table S1**).
190 Interestingly, these two mutations were found together in 100% of the viral sequences, suggesting
191 potential co-evolution (**Fig. S1O**). They have also been reported as positively selected in the
192 context of sub-optimal neutralizing antibody concentration (216KLRS) (*7*) or in the context of
193 cross-species adaptation (216KLRS and R245H) (*8*). Despite the lack of humoral responses,
194 these findings underscore how BLT-L mice can recapitulate host-pathogen interactions that drive
195 SARS-CoV-2 evolution and host adaptation.
196
197 **Systemic depletion of CD4+ cells abrogates viral clearance in fLX.**
198 The addition of a human thymus in the BLT-L model generates a more functional T
199 lymphocyte compartment. Therefore, we wished to examine the contribution of T cells in SARS-
200 CoV-2 infection resolution. We performed systemic depletion of CD3+, CD4+, and CD8+ cells
201 through the administration of OKT3, OKT4, or OKT8 depleting antibodies, respectively, via
202 intraperitoneal injection both prior to and after infection (**Fig. 2A**). Effective systemic depletion
203 was confirmed in the blood by flow cytometry (**Fig. S2A**). All animals were euthanized at 12 dpi
204 to assess for the persistence of SARS-CoV-2 infection in fLX. While depletion of CD3+, CD4+,
205 and CD8+ cells induced persistent infection in some or most of the animals, only CD4+ cell
206 depletion (mean Log PFU/mg tissue = 2.37) resulted in a statistically significant defect in infection
207 resolution compared to all other experimental conditions (isotype, OKT3, and OKT8-treated mice)

208 (**Fig. 2B**). The rate of productively infected fLX was also higher in CD4+ cell-depleted animals,
209 with 72% of fLX (8/11) showing infection at 12 dpi compared to 50% (4/8) and 33% (2/6) in CD3-
210 and CD8-depleted mice, respectively (**Fig. 2B**). Additionally, when examining the average viral
211 titer (Log PFU/mg of tissue) of persistently infected fLX, the ones from CD4+ cell-depleted animals
212 were significantly higher compared to CD3+ cell- depleted fLX (**Fig. S2B**), furthering that CD4+
213 cells have a more consequential impact on driving infection resolution than CD3+ cells. Anti-
214 SARS-CoV-2 N IHC confirmed these findings and superior defect of CD4+ cell-depleted animals
215 to resolve infection (**Fig. 2C**). Using multiplex fluorescent IHC (mIHC), we also validated the
216 reduction in CD3+, CD4+ and CD3+ CD4- cells in fLX from CD3-, CD4- and CD8-depleted
217 animals respectively, compared to isotype-treated animals (**Fig.2D**).

218 Persistent infection in CD4+ cell-depleted animals was also associated with significant
219 downregulation of MHC class I (**Fig. 2E**), a phenomenon we similarly observed in acutely infected
220 fLX (2 dpi) (**Fig. 2E**) and that has been previously reported in cells with active SARS-CoV-2
221 replication (*9, 10*). This further emphasizes that depletion of CD4+ cells is associated with
222 defective viral clearance mechanisms. These findings suggest that circulating CD4-expressing
223 cells, and to a lesser extent CD3+ T-cells, mediate SARS-CoV-2 infection resolution in BLT-L
224 mice.

225

226 **Human responses to SARS-CoV-2 mobilize specific hematopoietic subsets.**

227 To define the identity of the CD4+, and to a lesser extent, CD3+ subset(s) mediating
228 infection resolution, we performed single-cell RNA sequencing (scRNA-seq) on fLX from naïve
229 BLT-L mice and at 2 and 12 dpi. While most cells detected in fLX by scRNA-seq were human, a
230 minor population of mouse cells were detected, which were excluded from downstream analysis
231 (**Fig. S3A-C**). Analysis of the human compartment revealed diverse immune subsets (T
232 cells/innate lymphoid cells (ILC), B cells, myeloid cells and mast cells) and non-immune cell types
233 (ciliated and non-ciliated epithelial, endothelial, mesenchymal cells and chondrocytes) in both

234 naïve and infected fLX (**Fig. 3A-C and Fig. S3D,E**). It is important to note that because our tissue
235 digestion process and scRNAseq (in contrast to single nucleus RNAseq) both favor hematopoietic
236 cell characterization compared to non-immune compartments (11, 12), the recovery of non-
237 hematopoietic cell types is reduced, as evidenced by the limited number of cells in the epithelial
238 compartment. Regardless, the transcriptomic dynamics within each cell type, including
239 epithelium, could be examined upon infection.

240 Initial analysis showed that the transcriptomic response of the epithelial compartment
241 upon infection was consistent with previously reported signatures of patients suffering from
242 COVID-19 (*11-13*). Indeed, we noted a relative reduction of the alveolar type 2 (AT2)
243 compartment at 2 dpi (25.6%) compared to naïve mice (73.1%), which was partially restored at
244 12 dpi (49.1%) (**Fig. 3D,E**). In contrast, the AT1 compartment increased at 2 dpi (9.89% compared
245 to 8.00% in naïve fLX), consistently with the ability of AT2 cells to differentiate into AT1 upon lung
246 damage (*14*). AT2 cells did not exhibit any robust antiviral responses (**Fig. 3F**) in accordance with
247 the absence of viral RNA in this compartment (**Fig. 3G**). Given the clear evidence of epithelial
248 infection in fLX at 2 dpi (**Fig. 1B**[b]), the significant cytopathic damages induced by SARS-CoV-2
249 in AT2 cells (*15*), which results in a marked reduction of the AT2 compartment upon infection ((*16*)
250 and **Fig. 3E**), likely precluded the isolation of infected AT2 cells following fLX digestion and single-
251 cell isolation. However, bystander, non-infected AT2 cells displayed previously reported COVID-
252 19 signatures found in humans, including downregulation of MHC genes (*HLA-C, HLA-B, and*
253 *HLA-DPB1)* and *CCL5* (a cytokine associated with immune recruitment during respiratory
254 infection) (**Fig. 3F**) (*17*). To summarize, fLX epithelium recapitulated previously reported features
255 of COVID-19 in humans, including downregulation of immune genes and antigen presentation,
256 and activation of tissue repair mechanisms.

257 Following epithelial benchmarking, we examined how the overall human immune system
258 mobilizes within infected fLX. T-cells and innate lymphoid cells (ILC) have the same transcriptional
259 programs, express TCR genes, and play similar effector functions (*18*). Their shared features

260 render them very challenging to distinguish by scRNAseq in small datasets and without TCR
261 sequencing information (*19*). We thus considered them together as part of a T-cell/ILC population.
262 T-cell/ILC frequency dramatically decreased in fLX upon infection (naïve, 66.8%; 2 dpi, 35.3%;
263 12 dpi, 21.8%), which is consistent with evidence that COVID-19 can induce lymphocyte depletion
264 (**Fig. 3B,C**). Notably, lymphopenia was not observed in the peripheral blood of BLT-L mice,
265 suggesting that lymphocyte depletion in fLX was not directly attributed to declining circulating
266 peripheral lymphocytes (**Fig. S3F)**. In contrast, myeloid (naïve, 9.94%; 2 dpi, 25.3%; 12 dpi,
267 22.2%) and B-cell subsets (naïve, 3.64%; 2 dpi, 5.38%; 12 dpi, 5.31%) relatively expanded upon
268 infection (**Fig. 3A-C**).

269 One myeloid and one T-cells/ILCs populations showed clear segregation by time point
270 (population A and B in **Fig. 3B**) and were specific to 2 dpi. Most notably, these two hematopoietic
271 sub-clusters were also highly enriched in viral RNA compared to other hematopoietic lineages
272 (population A and B; **Fig. 3G, H**). While mesenchymal subsets also exhibited high levels of viral
273 reads (**Fig. 3G**), reads were limited and distributed sporadically without significant enrichment
274 within a given sub-cluster (**Fig. 3H and Fig. S3G**), including a 2 dpi-specific mesenchymal sub-
275 cluster (Population C; **Fig. 2B**), underscoring a lack of association between viral RNA and
276 mesenchymal activation upon SARS-CoV-2 challenge. Given their high enrichment in viral RNA
277 and temporal association with acute viral replication, this initial transcriptomic analysis highlights
278 the 2 dpi-specific myeloid and T-cells/ILCs populations identified as significant candidates in our
279 search for the cellular mediators of infection resolution.

280

281 **Inflammatory monocytes are major drivers of myeloid antiviral responses upon infection.**

282 Next, we wished to examine more closely the transcriptomic profile of the viral RNA
283 positive-myeloid and T/ILC populations. Since CD4+ cell depletion had a statistically significant
284 impact on infection resolution compared to CD3+ cell depletion (**Fig. 2B**), and given that human
285 monocytes, as well as some macrophages and dendritic cells (DC), also express CD4 (*20, 21*),

286 we first focused our study on the myeloid compartment. Sub-clustering of myeloid lineages
287 unveiled diverse subpopulations, including alveolar and interstitial macrophages, various
288 monocytes subsets, and one conventional DC subset (cDC) (**Fig. 4A and Fig. S4A-C**). Notably,
289 we found the 2 dpi-specific viral RNA-enriched myeloid subset, earlier referred to as population B
290 (**Fig. 4A-C and Fig. 3B,H**), to bear a signature of inflammatory monocytes (iMO) (**Fig. 4A,D-G**
291 **and Fig. S4D**). iMO exhibited elevated expression of *VCAN, S100A8, CD14, CD163* and
292 absence/minimal expression of *CD4, MARCO and CD206 (MRC1)* (**Fig. 4D-F and Fig. S4D)**.

293 Only iMO and alveolar macrophages increased in frequencies upon acute infection,
294 whereas cDC and interstitial macrophage frequencies decreased (**Fig. 4G**). iMO were the most
295 abundant lineage at 2 dpi (33.5%; **Fig. 4G**) and were the leading mediators of antiviral responses,
296 as exemplified by the robust upregulated expression of interferon-stimulated genes (ISGs) and
297 inflammatory cytokines (*CCL8, CXCL10, CCL2, ISG15, DEFB1, IL1RN, IFIT1, ISG20, IFIT3,* and
298 *MX1*), as well as inflammatory markers such as *CD163* (**Fig. 4D,H**). While some ISGs (e.g.,
299 *ISG15, IFIT3, and MX1*) were expressed in other myeloid lineages at 2 dpi, their expression was
300 markedly lower compared to iMO, suggesting a strong association between viral RNA and
301 potentiated antiviral responses. Notably, upregulation of *CCL8*, *CXCL11* and *DEFB1* transcripts
302 were the most exclusive to iMO (**Fig. 4H**).

303 As a side note, we also examined whether viral RNA-associated iMOs (CoV-iMOs)
304 displayed a specific transcriptomic signature compared to iMOs (noCoV-iMOs) with undetectable
305 viral RNA. Notably, only two genes correlated with the presence of viral RNA in iMOs: *FGL2 and*
306 *C15orf48* (**Fig. 4I**). While *FGL2* was down-regulated in CoV-iMO compared to noCoV-iMOs,
307 *C15orf48* was upregulated. Soluble FGL2 exerts immunosuppressive functions (notably by
308 inhibiting the NF-kB pathway) (*22*). Conversely, the mitochondrial protein C15orf48 is positively
309 regulated by NF-kB signaling (*23*) and has previously been implicated in severe COVID-19, acting
310 as a positive regulator of inflammation (*24*).

311 These findings underscore CD163+ iMO as major mediators of antiviral responses within
312 myeloid subsets and suggest that productive or abortive SARS-CoV-2 infection could further
313 potentiate iMO inflammation through a specific set of genes.
314
315 **iMO are extravascular and derive from patrolling CD4+ monocytes**
316 As iMO could contribute to infection resolution in BLT-L mice, we sought to understand
317 the origin of this transient cell subset using scRNA-seq, and cross-validate our findings using
318 mIHC approaches. We found that low expression of *CD4* was a defining feature of iMO amongst
319 monocyte sub-lineages (**Fig. 4E**), suggesting that iMO differentiation may be associated with loss
320 of *CD4* expression. In parallel to this observation, we noted a large population of *CD4+ CD163-*
321 *CD206(MRC1)*-patrolling intravascular monocyte (PIM) at all time points (**Sub-cluster 0**; **Fig.**
322 **4A,D-F**), with 2 dpi-specific PIM harboring a transcriptomic signature bridging naïve PIM and 2
323 dpi-specific iMO. At 12 dpi, PIM was the dominant subset over other monocyte subsets (50.3%;
324 **Fig. 4G**). These results suggest that the infiltration and activation of PIM in fLX upon infection
325 gives rise to a transient CD163+ iMO population contributing to infection resolution (**Fig. 4J**).
326 Analysis of myeloid chemotaxis transcriptomic signatures was consistent with increased
327 monocyte infiltration into fLX upon infection. Productive infection of fLX at 2 dpi resulted in the
328 emergence of cell subsets expressing high levels of human *CCL2* (**Fig. S4E**), which include our
329 CD163+ iMO subset and a 2 dpi-specific T-cells/ILCs sub-cluster (population A in **Fig. 3B**).
330 Activation of alveolar macrophages upon acute infection was also associated with increased
331 *CCL2* expression by these cells (**Fig. S4E**). Several transcripts involved in myeloid chemotaxis,
332 such as CXCR4 and MCAM (25, 26), were also upregulated in activated, 2 dpi-specific endothelial
333 cell sub-cluster (**Fig. S4G-I**), underscoring the potential contribution of the endothelium in myeloid
334 recruitment.
335 In support of our transcriptomic findings, mIHC analysis revealed that while naïve fLX
336 displayed high numbers of CD3+ cells and detectable CD163+ interstitial cells (likely

337 macrophages), acute infection at 2 dpi showed an increase in CD4- CD163+ cells both in the
338 extravascular interstitium and alveolar spaces (**Fig. 4K**). These dynamics mirrored the 2 dpi-
339 specific expansion of CD4- CD163+ iMO and alveolar macrophages uncovered through scRNA-
340 seq (**Fig. 4G**). A significant number of CD4+ CD3- CD163- cells were also apparent at that time
341 point by mIHC (**Fig. 4K**), which is consistent with the identification of CD4+ CD163- PIM at 2 dpi
342 by scRNAseq (**Fig. 4B,D,E**). Reduction of CD3+ T-cell was also apparent at 2 dpi (**Fig. 4K**) in
343 accordance with our scRNAseq findings (**Fig. 3C**). At 12 dpi, CD3- CD4+ cells were still noted in
344 fLX (**Fig. 4K**), reflecting the expansion of CD4+ PIM observed by scRNAseq (**Fig. 4G**). A
345 significant number of CD163+ cells were still observed in fLX at that time point (**Fig. 4K**) but
346 mainly concentrated in the interstitium, consistent with our scRNA findings that an increase in
347 CD163+ interstitial macrophages may concur simultaneously with the reduction in CD163+ iMO
348 numbers (**Fig. 4G**).

349 Concomitant to a recent study reporting that PIM give rise to a non-classical, extravascular
350 monocyte population in the mouse lung that expand upon stimuli (*25*), our mIHC and scRNA-seq
351 findings collectively suggest that infiltration of CD4+ PIM in infected fLX precede PIM
352 extravasation and differentiation into extravascular iMO. In further support of this extravascular
353 nature of iMO, the iMO gene expression profile was similar to those of human FCN1-monocytes
354 recovered from the broncho-alveolar lavage of COVID-19 patients with acute respiratory disease
355 syndrome (*26*), overall strengthening the non-classical, extravascular monocyte nature of iMO
356 and their human relevance in COVID-19. Extravascular iMO are referred to as ExiMO in the rest
357 of our study.

358

359 **CD4+ cell depletion disrupts CD163+ cell recruitment into productively infected fLX.**

360 Productive fLX infection at 2 dpi is associated with a significant increase in CD163+ cells
361 in fLX (**Fig. 4K**), which is dominantly attributed to ExiMO differentiation as per our scRNA-seq
362 data (**Fig. 4B,D**). At 12 dpi, the overall amount of CD163+ cells in fLX remained high (**Fig. 4K**)

363 and was not statistically different from the amount of CD163+ cells observed at 2 dpi (**Fig. 5A,B**),
364 which is likely the manifestation of the presence of residual ExiMO and of the differentiation of
365 CD163+ CD206+ interstitial macrophages from infiltrating CD4+ CD14+ CD16- monocytes at 12
366 dpi (**Fig. 4D,G**) consistently with the literature (*27*). As our data support a model in which
367 infiltrating CD4+ PIM differentiate into CD163+ ExiMO and interstitial macrophages upon and
368 following infection respectively, we examined how CD4+ cell depletion impacts CD163+
369 recruitment in fLX. Of note, because of the limited accessibility of fetal tissues and of a conscious
370 choice to limit our use of such tissue as much as possible, we restricted our analysis to a single
371 time point. We chose to focus our analysis on phenotypes observed at 12 dpi to ensure their
372 association with persisting infection (in contrast to acute infection).

373 Following CD4+ cell depletion, persistently infected fLX displayed a significantly reduced
374 number of CD163+ cells in fLX compared to isotype-treated and non-treated mice at 12 dpi (**Fig.**
375 **5A,B**). Expectedly, a major reduction was observed in the interstitial space (**Fig. 5A**), consistently
376 with reduced numbers of ExiMO and interstitial macrophages. Limited numbers of alveolar
377 CD163+ cells were still observed in the fLX of CD4+ cell-depleted mice co-localized with PPARγ
378 (**Fig. 5A**), a marker of lung alveolar macrophages, which are unlikely to be depleted by anti-CD4
379 antibodies consistently with the known limited accessibility of alveolar macrophages to systemic
380 antibodies (*28*). Despite being both similarly infected, fLX of acutely infected mice (2 dpi) also
381 displayed significantly higher numbers of CD163+ cells than persistently infected fLX (12 dpi)
382 (**Fig. 5A,B**). These findings support evidence that CD4+ cell depletion prevents monocyte
383 infiltration into fLX during and following infection, and consequentially any differentiation into
384 CD163+ cells. Notably, systemic levels of human CCL2 and CCL3, major monocyte attractants,
385 were elevated in CD4+ cell-depleted mice and comparable to those of acutely infected mice (**Fig.**
386 **5C**), underlining how defective CD163+ recruitment stems from a lack of circulating CD4+ cells
387 rather than reduced chemotaxis. Together, our findings therefore suggest that CD4+ cell depletion
388 abrogates the recruitment of ExiMO in infected fLX.

389

390 **Depletion of CD4+ cells in BLT-L mice promotes an immune tolerance state defined by the**
391 **lack of CXCL10 production**

392 To further support a link between CD4+ cell depletion, persistent infection and lack of
393 ExiMO differentiation, we compared antiviral responses during acute and persistent infection.
394 Among 32 cytokines and chemokines analyzed in the peripheral blood, CXCL10 was the only
395 cytokine displaying significantly increased serum levels in acutely infected mice (2 dpi) prior to
396 returning to undetectable levels upon infection resolution (12 dpi) (**Fig 5D**). However,
397 interestingly, levels of circulating human CXCL10 in persistently infected CD4+ cell-depleted mice
398 were not statistically different than those of mice that resolved infection (12 dpi) (**Fig 5D**),
399 suggesting that CD4+ cell depletion promotes a state of immune tolerance that favors viral
400 persistence. These findings also underscore systemic CXCL10 as a biomarker of viral clearance.

401 Several human subsets within fLX express *CXCL10* upon acute infection, including
402 myeloid, mesenchymal and endothelial subsets (**Fig. S5A,B**). Among mesenchymal subsets,
403 activated fibroblasts were enriched in *CXCL10* transcripts (**Fig. S5C-E**) unlike activated
404 endothelial cells (**Fig. S4I**). However, the myeloid compartment was the major source of *CXCL10*
405 among all human clusters at 2 dpi (**Fig. S5A,B**) and this phenotype was dominantly driven by
406 ExiMO (**Fig. 4H, S5B**). These observations underscore ExiMO as the dominant producer of
407 CXCL10 upon acute infection and as a significant source of this potential biomarker of infection
408 resolution.

409 Taken together, our results suggest that CD4+ cell depletion prevents the induction of
410 antiviral cytokines (i.e., CXCL10) dominantly expressed by ExiMO, resulting in a state of immune
411 tolerance that likely favor viral persistence. Combined with evidence that such a depletion
412 abrogates the recruitment of CD163+ cells into fLX upon infection and that ExiMO are the
413 dominant CD163-expressing cell population differentiating upon acute infection, these findings
414 collectively underscore ExiMO as critical mediators of infection resolution.

415

416 **Persistent infection is associated with systemic and local signatures of chronic infection.**

417 To probe whether CD4+ cell depletion and the lack of CD163+ cell recruitment drive long-
418 lasting viral persistence instead of simply delaying infection resolution, we investigated whether
419 immune tolerance in CD4+ cell-depleted mice is associated with signatures of chronic infection.
420 Notably, persistently-infected mice antiviral responses were distinguishable from acutely infected
421 (2 dpi) and isotype-treated (12 dpi) mice by elevated levels of CCL19 in serum (**Fig. 5E**). CCL19
422 is a pro-inflammatory cytokine that has been linked with persistent viral replication and
423 inflammation such as in the context of HIV-1 infection (*29*), underlining that persistent SARS-CoV-
424 2 infection in BLT-L mice recapitulate key immunological features of chronic viral infection.

425 We have previously reported that fLX exhibit significant histopathological manifestations
426 of disease upon SARS-CoV-2 infection in the absence of an engrafted human immune system
427 (3), highlighting that tissue damage in fLX is virally induced. However, persistent infection did not
428 result in any significant histopathological manifestations of disease in fLX, which strongly
429 contrasts with acutely infected fLX (**Fig. 1D, Fig. 5F**). As minimal tissue damage is a hallmark of
430 chronic viral infection (*30*), these findings further support evidence that CD4+ cell depletion
431 promotes tissue remodeling processes underlying chronic infection and lasting viral persistence.

432

433 **Macrophage-like T-cells are enriched in viral RNA and mount robust antiviral signatures.**

434 Lastly, we aimed to complete our study by characterizing the 2 dpi-specific T-cell/ILC sub-
435 cluster emerging upon acute infection (population A in **Fig. 3B**), as CD3+ cell depletion had a
436 moderate, albeit non-significant, impact on infection resolution (**Fig. 2B**). T-cell/ILC responses
437 were limited to this specific subpopulation (**Fig. 6A,B**), which clustered very distinctively from
438 other CD3+ T-cell lineages, including canonical CD4+ and CD8+ T-cells, and was highly enriched
439 in viral RNA (Sub-cluster 6; **Fig. 6A-C**). Cells included in this subpopulation displayed low levels
440 of CD4 and CD8 transcripts and elevated levels of mitochondrial transcripts **(Fig. 6E; Fig. S6A,B**).

441 Most notably, this T-cell/ILC subset was uniquely defined by the expression of several transcripts
442 known to be enriched in macrophages (*MARCO*, *TIMP1*, *LYZ*), fibroblasts (*MGP*, *CALD1*,
443 *COL1A*), or both (*A2M*, *IFITM3*) but not in T-cells (**Fig. 6E and Fig. S6D**). Cells included in this
444 subset also exhibited evidence of cytotoxic function through the expression of *GZMA*, *GZMB*, and
445 GNLY transcripts, albeit expression was also detected in CD8+ T-cells and activated tissue-
446 resident memory T-cells (TRM) (Sub-clusters 1,3,4, **Fig. 3E and Fig. S3D**). Given the proximity
447 of this sub-cluster with myeloid lineages (**Fig. 3A,B**) and evidence of expression of macrophage-
448 enriched transcripts, we referred to this unique sub-cluster as Macrophage-like T-cells (MTC).
449 MTC also exhibited upregulation of key gene pathways related to COVID-19, SARS-CoV-2 cell-
450 intrinsic immune responses, cellular cytotoxicity (e.g., degranulation) and cell death, consistently
451 with a role for this subset to serve as a robust primary responder to viral infection. (**Fig. 6D**).
452 Collectively, these findings suggest a potential link between our CD3+ cell-depletion findings and
453 the innate antiviral responses of CD3+ MTC.
454

455 **DISCUSSION**

456 As our appreciation of the immunological differences between mice and humans continues
457 to grow, humanized mouse models are increasingly standing out as robust platforms to
458 understand how viral pathogens interact with human tissues and the human immune system.
459 These models are especially valuable when investigating tissue and mucosal immunity since such
460 investigations remain impractical in human patients.

461 The SARS-CoV-2 pandemic has emphasized the need to increase our understanding of
462 immune mechanisms that can drive protection against immunologically novel respiratory viruses.
463 Mice engrafted with human immune systems and human lung tissues have emerged as valuable
464 tools for such investigations (*2-5*), bridging the limitations of conventional animal models and the
465 challenges associated with human studies. We previously reported using the HNFL mouse model
466 that such models can be leveraged to capture immunological signatures defining effective control

467 of SARS-CoV-2 infection (*3*). However, the enhanced myeloid reconstitution of the HNFL model
468 rapidly inhibits viral replication in fLX, precluding our ability to study protective naive
469 immunological mechanisms at play upon acute and potentially symptomatic infection. This study
470 aimed to uncover novel facets of these mechanisms using an alternative humanized mouse model
471 that exhibits robust susceptibility to acute hERV infection and a robust ability to resolve infection
472 in a hematopoietic-dependent manner.

473 We found that BTL-L mice are able to effectively clear both infectious viral particles and
474 viral RNA following an early peak of viral replication in fLX. Systemic depletion of CD4+, but not
475 CD3+ or CD8+ robustly abrogates infection resolution, underlining the contribution of the human
476 hematopoietic compartment in this process. This is consistent with evidence that immunodeficient
477 mice only engrafted with fLX are unable to clear infection (*3, 31*). Leveraging scRNAseq
478 approaches, we uncovered ExiMO as a transient and novel subset of extravascular monocytes.
479 ExiMO are directly related to CD4+ PIM and are the dominant CD163-expressing myeloid subset
480 to emerge in fLX upon acute viral replication. They are also highly enriched in viral RNA and
481 display unique antiviral and myeloid transcriptomic signatures. Notably, CD4+ cell depletion
482 abrogates CD163+ infiltration in fLX despite persisting viral replication and promotes a state of
483 immune tolerance defined by the lack of an antiviral cytokine, CXCL10, defining effective infection
484 resolution and dominantly expressed by ExiMO. Lastly, we uncovered that CD4+ cell depletion is
485 also associated with signatures of chronic infection systemically and in fLX.

486 All of our findings unequivocally converge toward a critical role of ExiMO in driving infection
487 resolution in fLX. These cells belong to the only subset displaying the four following features: 1)
488 a dominant CD163-expressing population that emerge during acute infection, 2) a major source
489 of *CXCL10* expression, 3) a high enrichment in viral RNA and 4) the induction of robust antiviral
490 responses. Our study therefore unravels ExiMO recruitment into lung tissues as a critical
491 immunological process driving effective infection resolution and prevention of chronic infection.
492 Notably and to the best of our knowledge, our study represents the first evidence of a lung

493 monocyte extravascular subset with antiviral functions. Extravascular monocytes are known to
494 originate from circulating patrolling monocytes and have been proposed to serve as immune
495 sentinels through their position at the interface of the lung capillaries and alveoli(*25, 32*). However,
496 although previous research reported that these cells can promote T-cell resident memory
497 differentiation following viral infection (*33*), their direct antiviral functions have not been
498 documented until now.
499
500 Our study collectively illuminates a novel immunological model that may–in part–define
501 naïve antiviral immunity against SARS-CoV-2 and potentially other hERVs in the human lung
502 (**See Graphical Abstract**). We propose that upon infection of fLX, initial epithelial infection
503 triggers the activation of fibroblasts and endothelial cells. While fibroblasts potentiate initial
504 myeloid inflammatory responses, endothelial activation, and CCL2 production by several
505 activated subsets (of mesenchymal and myeloid origin) promote PIM infiltration into fLX. Following
506 extravasation, PIM then subsequently differentiate into ExiMO, which may exert a bimodal
507 function: they drive tissue-wide antiviral responses protecting the epithelial compartment from
508 persistent infection, and phagocyte viral particles and components, heightening their antiviral
509 responses. Infection resolution is associated with a significant reduction of ExiMO in fLX,
510 subsequent infiltration of PIM and differentiation into CD206+ interstitial macrophages which
511 promote tissue repair. By preventing PIM infiltration into fLX and subsequent ExiMO differentiation
512 and antiviral responses, CD4+ cell depletion promotes a state of immune tolerance driving long-
513 lasting viral persistence.
514 Through such model, our findings significantly enhance a recent human study reporting
515 that protection from SARS-CoV-2 infection is associated with a rapid monocyte response in the
516 nasal cavity and a decreased number of circulating monocytes(*1*). Specifically, our work extends
517 the findings of this human study beyond the limitations of the human model by exploring tissue-
518 resident events, unraveling the identity of monocyte populations that extravasate tissues,

519 differentiate and mount tissue-resident immune responses to clear infection. By providing
520 enhanced resolution on key protective immunological processes and mediators that human
521 studies alone cannot capture, underscoring how human and humanized mouse studies can
522 effectively complement themselves for improving our understanding of human antiviral immunity.
523

524 While our study emphasizes the protective role of monocytes in preventing severe COVID-
525 19, monocytic lineages have also been extensively associated with severe COVID-19 (*11-13, 26*).
526 Excessive monocyte infiltration, macrophage inflammation and fibrotic response can lead to
527 potentially fatal acute respiratory distress syndrome (ARDS) and fibrosis despite promoting
528 infection resolution. A suspected driver of excessive myeloid inflammation is the ability of SARS-
529 CoV-2 to trigger abortive infection of both monocytes and macrophages (*34-37*) through viral RNA
530 replication and protein production, which results in inflammasome activation (*37-39*). However,
531 viral RNA in ExiMO is associated with rapid infection resolution and tissue protection. These
532 findings suggest that monocytic infection can also be associated with positive clinical outcomes
533 and that the inflammatory trajectory of infected monocytes may define the course of COVID-19.
534 By 12 dpi and infection resolution, fLX displayed residual ExiMO and were enriched in
535 CD4+ PIM and CD163+ CD206+ interstitial macrophages. These findings are consistent with
536 mouse studies reporting that CD206+ interstitial macrophages are involved in response to
537 wounding and infection recovery, while CD206- interstitial macrophages are primary responders
538 to infection and more pro-inflammatory (*25*). However, human patients experiencing severe
539 COVID-19 and ARDS display an accumulation of pro-fibrotic CD163+ CD206+ monocyte-derived
540 interstitial macrophages (*26*). These cells have been shown to directly derive from extravasating,
541 circulating CD14+ monocytes in another human immune system-engrafted mouse model(*27*),
542 suggesting that exacerbated monocyte infiltration and differentiation into CD206+ interstitial
543 macrophages are a significant driver of COVID-19 disease as viral infection is being cleared in
544 lung tissues. In addition to this, other studies have reported that PIM can give rise to lung

545 extravascular monocytes in mice (*25*). These cells exhibit a dynamic transition state and can
546 differentiate into CD206- interstitial macrophages. However, notably, no CD206- macrophages
547 were observed in infected fLX at any time point. Together, these findings suggest that the absence
548 of ExiMO differentiation into CD206- interstitial macrophages during infection represents a
549 defining hallmark of protection from severe COVID-19. Limited differentiation would avert
550 uncontrolled and imbalanced inflammation during infection resolution, preventing severe tissue
551 damage and subsequent exacerbated monocyte differentiation into pro-fibrotic CD206+ interstitial
552 macrophages (**Figure 7**). Together, our study suggests that ExiMO antiviral responses represent
553 a critical crossroad that can shape the clinical trajectory of SARS-CoV-2 infection.
554
555 Our findings call for numerous follow-up investigations. Understanding the cellular and
556 molecular actors defining the fate of ExiMO upon exposure to SARS-CoV-2 and how key
557 regulatory crossroads in this subset may result in differential clinical outcomes is of particular
558 interest. Compounding immune dysregulations, such as elevated inflammatory baseline and/or
559 specific myeloid imprinting, may contribute to PIM and/or ExiMO's inability to adequately regulate
560 their activation in a timely manner upon encountering viral materials or inflammatory clues,
561 leading to rapid differentiation into macrophages and exacerbated inflammation. Our study also
562 creates a mandate for probing the ubiquitous nature of ExiMO antiviral responses during other
563 respiratory viral infections and investigating more comprehensively the antiviral functions of this
564 novel subset beyond SARS-CoV-2 infection. Investigating the contribution of endothelial
565 activation in driving effective monocyte infiltration and infection resolution, as well as these cells'
566 contribution to ExiMO differentiation, is also of particular significance. It remains unclear as to
567 how endothelial and fibroblasts are activated during infection as neither cell population displayed
568 signs of viral RNA enrichment. Whether activation of these cells is triggered indirectly by early
569 epithelial and/or myeloid activation, or via direct exposure to viral components such as the
570 nucleocapsid protein (*40*) could be investigated using the BLT-L mouse model.

571

572 In parallel to ExiMO, we also identified MTC, a transient T-cell population highly enriched
573 in viral RNA and only observed upon acute infection. MTC exhibited expression of key
574 macrophage-defining genes and elevated cytotoxic activity. While this population presents some
575 similarity with innate-like T-cells (*41*), which harbor cytotoxic signatures and whose roles in cancer
576 have been investigated, MTC appear to be unique given their combination of lymphoid, myeloid
577 and mesenchymal markers and their short-lived, apoptotic nature suggested by their complete
578 absence at 12 dpi. MTC also share transcriptomic similarities with γδ T-cell subsets previously
579 described as bearing myeloid and cytotoxic functions (*42, 43*). However, their expression of
580 conventional macrophage makers emphasizes their uniqueness. While CD8+ T-cells and
581 macrophages isolated from nasopharyngeal swabs have been identified to harbor SARS-CoV-2
582 RNA in human challenge studies(*1*), MTC did not meet the canonical transcriptomic signatures of
583 these subsets, suggesting the existence of tissue-resident events driving specific cellular
584 differentiation processes upon infection. Additional investigations are required to better
585 understand the identity, fate and functions of this novel cell subset in lung antiviral immunity.
586 However, it is tempting to speculate that MTC may uniquely synergize CD8+ cytotoxic T-cell
587 functions with viral particle phagocytosis to effectively control infection prior to undergoing rapid
588 cell death.

589 Despite our findings related to MTC, the contribution of T-cells in SARS-CoV-2 infection
590 resolution remains elusive in our model. CD3+ cell depletion resulted in a partial abrogation of
591 infection resolution, with 50% of animals still capable of clearing infection. In addition, even when
592 viral infection persisted in CD3+ cell-depleted animals, viral titers in fLX remained significantly
593 lower than in the fLX of persistently infected CD4+ cell-depleted animals (**Fig. S2B**). One possible
594 interpretation is that T-cell depletion delays but does not abolish infection resolution. CD8+ cell-
595 depleted mice may display delayed viral clearance compared to isotype-treated mice (with
596 resolution occurring between 6 dpi and 12 dpi), and CD3+ T-cell-depleted mice may be

597 undergoing progressive resolution by 12 dpi until complete clearance by a later time. In contrast,
598 the viral titer observed in fLX of CD4+ cell-depleted mice show no evidence of ongoing infection
599 resolution. How CD3+ depletion may impact MTC differentiation, and how T-cells (including MTC)
600 and ExiMO functions may synergize to rapidly resolve infection without extensive inflammation-
601 induced tissue damage will need further investigation.
602
603 There are inherent limitations associated with the BLT-L mouse model. First, direct viral
604 inoculation into fLX potentially bypasses key immune checkpoints in the upper respiratory tract,
605 which are not recapitulated in our model. Second, the hematopoietic reconstitution and functions
606 of the BLT-L mouse model remain imperfect, notably through the underrepresentation of specific
607 hematopoietic subsets, including dendritic cells and granulocytes, and limited B-cell responses –
608 which may ultimately bias the dynamics of viral clearance. Despite these limitations, BLT-L mice
609 recapitulated human lung responses to SARS-CoV-2 infection through AT2 loss of programming,
610 fibroblast and endothelial activation, effective clearance of infection through robust hematopoietic
611 responses. This mouse model also supported viral adaptation processes with public health
612 relevance, and recapitulated signatures of persistent viral replication observed in patients
613 suffering from chronic infection. Our work demonstrates the potential of the BLT-L mouse model
614 to uncover naïve immune mechanisms and mediators governing the effective resolution of lung
615 infection by SARS-CoV-2. Our findings open avenues for a comprehensive examination of the
616 antiviral roles of ExiMO against hERV, which may pave the way toward innovative immunotherapy
617 strategies against these pathogens.
618
619 **AUTHOR CONTRIBUTIONS**
620 D.K., A.B.B. and F.D. conceptualized the overall study. C.H. conceptualized the computational
621 component of this study and oversaw the analysis of the single-cell RNA sequencing data. D.K.,
622 A.B.B., N.A.C. and F.D. designed the experiments. D.K., A.K.O., M.S, A.N, H.P.G., M.E., V.V.,

623 A.B.B. and F.D. performed experiments. D.K., A.K.O., A.T., J.T., M.S, A.N, P.M., M.E., J.H.C.,
624 V.V., N.A.C., C.H., A.B.B. and F.D. analyzed the data. J.T and C.H. carried out computational
625 analysis. M.E. carried out electron microscopy analysis. A.B.B. and V.V. provided access to key
626 resources. D.K. and F.D. wrote the manuscript with contributions from all authors.
627

628 **ACKNOWLEDGMENTS**

629 This work was supported in part by a start-up fund and Peter Paul Career Development
630 Professorship from Boston University (to F.D.), grants from the National Institutes of Health (K22
631 AI144050 to F.D.), Clinical and Translational Science Awards (grant UL1 TR001430) from the
632 National Center for Advancing Translational Sciences of the National Institutes of Health (to F.D.,
633 N.A.C. and A.E.), and an Evergrande MassCPR award (to R.B.). A.B.B. was supported by
634 R01AI174875, R01AI174276, DP2DA040254, as well as CDC subcontract 200-2016-91773-
635 T.O.2. and a Massachusetts Consortium on Pathogenesis Readiness (MassCPR) grant. We also
636 thank the Evans Center for Interdisciplinary Biomedical Research at Boston University Chobanian
637 and Avedisian School of Medicine for their support of the Affinity Research Collaborative on
638 'Respiratory Viruses: A Focus on COVID19'. This work utilized a Ventana Discovery Ultra and
639 Akoya PhenoImager HT that were purchased with funding from National Institutes of Health SIG
640 grants (S10 OD026983 & S10OD030269). We thank Ronald B. Corley, NEIDL director at the time
641 of this study and MassCPR award recipient, for his constant encouragement and support for this
642 study. We thank the Boston University Animal Science Center, the Ragon Institute Human
643 Immune System Mouse core, the single cell sequencing core and microarray and sequencing
644 core, and the flow cytometry core at Boston University Chobanian and Avedisian School of
645 Medicine, and all the NEIDL animal core staff for their outstanding support. We also thank all the
646 Douam, Balazs, Connor and Crossland lab members, NEIDL members, and members of the
647 department of Virology, Immunology, and Microbiology and Pathology at Boston University for

their constant support and advice. D.K. is supported by a T32 training grant in immunology (T32AI007309).

MATERIALS AND METHODS

Detailed descriptions of the materials and methods used for this study are in the Supplemental Materials.

Study design. Three independent cohorts of BLT-L mice co-engrafted with human fLX, liver, thymus and hematopoietic stem cells from three distinct donors were generated for this study. Animals were challenged with SARS-CoV-2 (10^6 PFU) through direct fLX inoculation, and euthanized on day 2, 6 or 12 post-infection for blood and fLX collection. Naïve mice were used as negative controls. fLX were then processed for viral titer quantification, H&E staining and mIHC, scRNAseq and viral genome sequencing. Blood was processed for flow cytometry (for depletion experiments only) and serum cytokine analysis. For CD3+, CD4+ and CD8+ cell depletion, mice were treated with depleting antibodies prior and during infection through intraperitoneal injection.

Institutional approvals. All experiments in this study, including those conducted in BSL-3, were approved by an institutional biosafety committee. Animal experiments described in this study were performed in accordance with protocols that were reviewed and approved by the Institutional Animal Care and Use and Committee of the Ragon Institution and Boston University. All mice were maintained in facilities accredited by the Association for the Assessment and Accreditation of Laboratory Animal Care (AAALAC). All replication-competent SARS-CoV-2 experiments were performed in a biosafety level 3 laboratory (BSL-3) at the Boston University National Emerging Infectious Diseases Laboratories (NEIDL).

673

674 ***Mouse strains and sex as biological variable.*** Female NOD.Cg.-*Prkdc*^{Scid}*Il2rg*^{tm1Wjl}/SzJ (NSG)
675 mice were obtained from the Jackson Laboratory, catalog number 005557. NSG mice were
676 maintained by the Ragon Institute Human Immune System Mouse core prior to engraftment and
677 shipment to the NEIDL, Boston University. In our study, only female mice were engrafted with
678 human fetal tissues because of their ability to support higher levels of engraftment than males.
679 As we investigated human tissue responses to infection and only leveraged mice as
680 xenorecipients, the sex of the animals does represent a critical variable for our study.

681

682 ***Human fetal tissues.*** De-identified human fetal tissues were procured from Advanced Bioscience
683 Resources (Alameda, CA, USA).

684

685 ***Generation of BLT-L mice.*** BLT mice were generated via irradiation of female NOD.Cg.-
686 *Prkdc*^{Scid}*Il2rg*^{tm1Wjl}/SzJ mice (NSG mice; Jackson Laboratory #005557) prior to implantation of
687 human fetal thymic and fetal liver tissue (Advanced Bioscience Resources) under the murine
688 kidney capsula. Two pieces of homologous human fetal lung tissue were implanted into
689 subcutaneous dorsal pockets of mice. Post-implantation, mice intravenously received $1x10^5$
690 homologous CD34+ cells. Human immune reconstitution was determined by flow cytometry at
691 weeks post-implantation. Three distinct human donors were used for this study.

692

693 ***Mouse inoculation with SARS-CoV-2.*** BLT-L mice were anesthetized with 1–3% isoflurane prior
694 to inoculation via subcutaneous, intra-fetal lung xenograft (intra-fLX) injection with 10^6 plaque
695 forming unites (PFU) of SARS-CoV-2 WA-1 isolate in 50 µL of sterile 1X PBS. Mice were
696 euthanized at 2-, 6-, and 12-days post inoculation.

697

698 ***In vivo antibody depletion.*** BLT-L mice were administered 200 mg of anti-CD3e (OKT3)
699 (BioxCell; cat. # BE0001-2), anti-CD4 (OKT4) (BioxCell; cat. # BE0003-2), anti-CD8 (OKT8)
700 (BioxCell; cat. # BE0004-2), or isotype IgG2a (Thermofisher; cat # 02-6200) antibody 3-, 2-, and
701 1-day prior to inoculation and 4- and 8-days post inoculation with $1x10^6$ PFU SARS-CoV-2 WA-
702 1.
703
704 ***Quantification and statistical Analysis.*** For histopathological score and viral load/titer
705 comparisons a Kruskla-Wallis, non-parametric one-way ANOVA with Benjamini, Krieger, and
706 Yekutieli correction for multiple comparisons was applied given the non-continuous nature of the
707 data. For cytokine data, an Ordinary one-way ANOVA with uncorrected Fishers LSD was used
708 as the data was collected from different time points, treatment conditions, and cohorts. A Kruskla-
709 Wallis, non-parametric one-way ANOVA with an uncorrected Dunn's test was applied for CD163+
710 Area quantification (AQ) due to the independent comparisons between the samples. All statistical
711 tests and graphical depictions of results were performed using GraphPad Prism version 9.0.1
712 software (GraphPad Software, La Jolla, CA). For all tests, $p \leq 0.05$ was considered statistically
713 significant. Statistical significance on figures and supplemental figures is labeled with p-values
714 and non-significant values are labeled with n.s. or left unlabeled.
715
716 ***Data availability***. The accession number for the raw data of the bulk and single-cell RNA-Seq is
717 GSE255200.
718
719 **REFERENCES**

720 1. R. G. H. Lindeboom *et al.*, Human SARS-CoV-2 challenge uncovers local and systemic
721 response dynamics. *Nature*, (2024).
722 2. Y. Di *et al.*, SARS-CoV-2 Variant-Specific Infectivity and Immune Profiles Are Detectable
723 in a Humanized Lung Mouse Model. *Viruses* **14**, (2022).
724 3. D. J. Kenney *et al.*, Humanized mice reveal a macrophage-enriched gene signature
725 defining human lung tissue protection during SARS-CoV-2 infection. *Cell Rep* **39**, 110714
726 (2022).

727 4. R. Sun *et al.*, Humanized mice for investigating SARS-CoV-2 lung infection and
728 associated human immune responses. *Eur J Immunol* **52**, 1640-1647 (2022).
729 5. A. Wahl *et al.*, Precision mouse models with expanded tropism for human pathogens. *Nat*
730 *Biotechnol* **37**, 1163-1173 (2019).
731 6. A. K. O'Connell, F. Douam, Humanized Mice for Live-Attenuated Vaccine Research: From
732 Unmet Potential to New Promises. *Vaccines (Basel)* **8**, (2020).
733 7. PMDA, Xevudy for Intravenous Infusion 500 mg_GlaxoSmithKline K.K._Report on Special
734 Approval for Emergency; https://www.pmda.go.jp/files/000245006.pdf. (2021).
735 8. A. Fagre *et al.*, SARS-CoV-2 infection, neuropathogenesis and transmission among deer
736 mice: Implications for spillback to New World rodents. *PLoS Pathog* **17**, e1009585 (2021).
737 9. N. Arshad *et al.*, SARS-CoV-2 accessory proteins ORF7a and ORF3a use distinct
738 mechanisms to down-regulate MHC-I surface expression. *Proc Natl Acad Sci U S A* **120**,
739 e2208525120 (2023).
740 10. J. S. Yoo *et al.*, SARS-CoV-2 inhibits induction of the MHC class I pathway by targeting
741 the STAT1-IRF1-NLRC5 axis. *Nat Commun* **12**, 6602 (2021).
742 11. T. M. Delorey *et al.*, COVID-19 tissue atlases reveal SARS-CoV-2 pathology and cellular
743 targets. *Nature*, (2021).
744 12. A. F. Rendeiro *et al.*, The spatial landscape of lung pathology during COVID-19
745 progression. *Nature* **593**, 564-569 (2021).
746 13. E. Wauters *et al.*, Discriminating mild from critical COVID-19 by innate and adaptive
747 immune single-cell profiling of bronchoalveolar lavages. *Cell Res* **31**, 272-290 (2021).
748 14. A. Wu, H. Song, Regulation of alveolar type 2 stem/progenitor cells in lung injury and
749 regeneration. *Acta Biochim Biophys Sin (Shanghai)* **52**, 716-722 (2020).
750 15. J. Huang *et al.*, SARS-CoV-2 Infection of Pluripotent Stem Cell-Derived Human Lung
751 Alveolar Type 2 Cells Elicits a Rapid Epithelial-Intrinsic Inflammatory Response. *Cell stem*
752 *cell* **27**, 962-+ (2020).
753 16. J. C. Melms *et al.*, A molecular single-cell lung atlas of lethal COVID-19. *Nature* **595**, 114-
754 119 (2021).
755 17. M. Liao *et al.*, Single-cell landscape of bronchoalveolar immune cells in patients with
756 COVID-19. *Nat Med* **26**, 842-844 (2020).
757 18. C. Harly, M. Cam, J. Kaye, A. Bhandoola, Development and differentiation of early innate
758 lymphoid progenitors. *J Exp Med* **215**, 249-262 (2018).
759 19. G. Pizzolato *et al.*, Single-cell RNA sequencing unveils the shared and the distinct
760 cytotoxic hallmarks of human TCRVdelta1 and TCRVdelta2 gammadelta T lymphocytes.
761 *Proc Natl Acad Sci U S A* **116**, 11906-11915 (2019).
762 20. A. Zhen *et al.*, CD4 ligation on human blood monocytes triggers macrophage
763 differentiation and enhances HIV infection. *J Virol* **88**, 9934-9946 (2014).
764 21. L. Jardine *et al.*, Rapid detection of dendritic cell and monocyte disorders using CD4 as a
765 lineage marker of the human peripheral blood antigen-presenting cell compartment. *Front*
766 *Immunol* **4**, 495 (2013).
767 22. L. Fu, Z. Liu, Y. Liu, Fibrinogen-like protein 2 in inflammatory diseases: A future
768 therapeutic target. *Int Immunopharmacol* **116**, 109799 (2023).
769 23. Y. Takakura *et al.*, Mitochondrial protein C15ORF48 is a stress-independent inducer of
770 autophagy that regulates oxidative stress and autoimmunity. *Nat Commun* **15**, 953 (2024).
771 24. S. A. Clayton *et al.*, Inflammation causes remodeling of mitochondrial cytochrome c
772 oxidase mediated by the bifunctional gene C15orf48. *Sci Adv* **7**, eabl5182 (2021).
773 25. J. Schyns *et al.*, Non-classical tissue monocytes and two functionally distinct populations
774 of interstitial macrophages populate the mouse lung. *Nat Commun* **10**, 3964 (2019).
775 26. D. Wendisch *et al.*, SARS-CoV-2 infection triggers profibrotic macrophage responses and
776 lung fibrosis. *Cell* **184**, 6243-6261 e6227 (2021).

27. E. Evren *et al.*, Distinct developmental pathways from blood monocytes generate human lung macrophage diversity. *Immunity* **54**, 259-275 e257 (2021).
28. T. Hussell, T. J. Bell, Alveolar macrophages: plasticity in a tissue-specific context. *Nat Rev Immunol* **14**, 81-93 (2014).
29. J. K. Damas *et al.*, Homeostatic chemokines CCL19 and CCL21 promote inflammation in human immunodeficiency virus-infected patients with ongoing viral replication. *Clin Exp Immunol* **157**, 400-407 (2009).
30. E. I. Zuniga, M. Macal, G. M. Lewis, J. A. Harker, Innate and Adaptive Immune Regulation During Chronic Viral Infections. *Annu Rev Virol* **2**, 573-597 (2015).
31. A. Wahl *et al.*, SARS-CoV-2 infection is effectively treated and prevented by EIDD-2801. *Nature* **591**, 451-457 (2021).
32. M. P. Rodero *et al.*, Immune surveillance of the lung by migrating tissue monocytes. *Elife* **4**, e07847 (2015).
33. P. R. Dunbar *et al.*, Pulmonary monocytes interact with effector T cells in the lung tissue to drive T(RM) differentiation following viral infection. *Mucosal Immunol* **13**, 161-171 (2020).
34. J. Zheng *et al.*, Severe Acute Respiratory Syndrome Coronavirus 2-Induced Immune Activation and Death of Monocyte-Derived Human Macrophages and Dendritic Cells. *J Infect Dis* **223**, 785-795 (2021).
35. A. Boumaza *et al.*, Monocytes and Macrophages, Targets of Severe Acute Respiratory Syndrome Coronavirus 2: The Clue for Coronavirus Disease 2019 Immunoparalysis. *J Infect Dis* **224**, 395-406 (2021).
36. D. Yang *et al.*, Attenuated Interferon and Proinflammatory Response in SARS-CoV-2-Infected Human Dendritic Cells Is Associated With Viral Antagonism of STAT1 Phosphorylation. *J Infect Dis* **222**, 734-745 (2020).
37. C. Junqueira *et al.*, FcgammaR-mediated SARS-CoV-2 infection of monocytes activates inflammation. *Nature* **606**, 576-584 (2022).
38. D. Munnur *et al.*, Altered ISGylation drives aberrant macrophage-dependent immune responses during SARS-CoV-2 infection. *Nat Immunol* **22**, 1416-1427 (2021).
39. E. Sefik *et al.*, Inflammasome activation in infected macrophages drives COVID-19 pathology. *Nature* **606**, 585-593 (2022).
40. Y. Qian *et al.*, Direct Activation of Endothelial Cells by SARS-CoV-2 Nucleocapsid Protein Is Blocked by Simvastatin. *J Virol* **95**, e0139621 (2021).
41. M. Molgora, M. Colonna, Innate-like T cells: A promising asset in anti-cancer immunity. *Cancer Cell* **40**, 714-716 (2022).
42. M. Lebedev, B. Faburay, J. A. Richt, A. Young, Myeloid-like gammadelta T cell subset in the immune response to an experimental Rift Valley fever vaccine in sheep. *Vet Immunol Immunopathol* **233**, 110184 (2021).
43. M. Muto, M. Baghdadi, R. Maekawa, H. Wada, K. Seino, Myeloid molecular characteristics of human gammadelta T cells support their acquisition of tumor antigen-presenting capacity. *Cancer Immunol Immunother* **64**, 941-949 (2015).

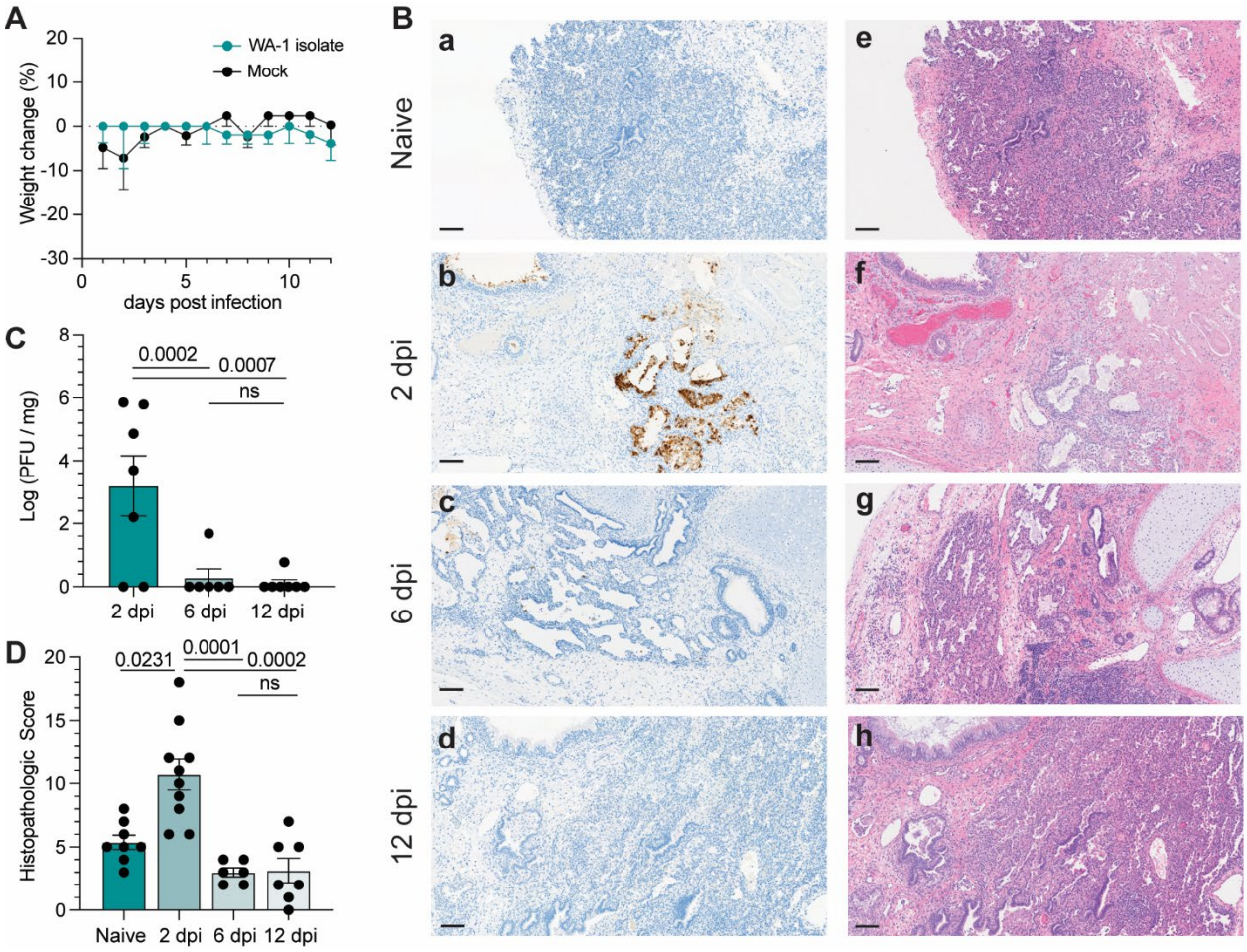

Figure 1. BLT-L mice effectively resolve SARS-CoV-2 infection and repair lung tissue. Fetal lung xenografts (fLX) of BLT-L mice were infected with $1x10^6$ PFU of SARS-CoV-2 WA-1 isolate via subcutaneous intra-graft injection. **(A)** BLT-L mice were monitored for weight change over the course of 12-days post infection (dpi). **(B)** Immunohistochemistry for SARS-CoV-2 S protein **(a-d)** and hematoxylin and eosin staining **(e-f)** were performed on naïve fLX **(a,e)** and fLX at 2 dpi **(b,f)**, 6 dpi **(c,g),** and 12 dpi **(d,h)**. Scale bar = 100 μM **(C)** Viral titer (log(PFU/mg)) in fLX at 2, 6, and 12 dpi as determined by plaque assay. **(D)** Histopathological scoring of naïve fLX and fLX at 2, 6, and 12 dpi. Data are representative of two or three independent experiments. n = 6 -10 per timepoint. Error bars represent mean ± standard error of the mean. *One-way ANOVA analysis was performed. p-values are indicated. n.s. = non-significant.*

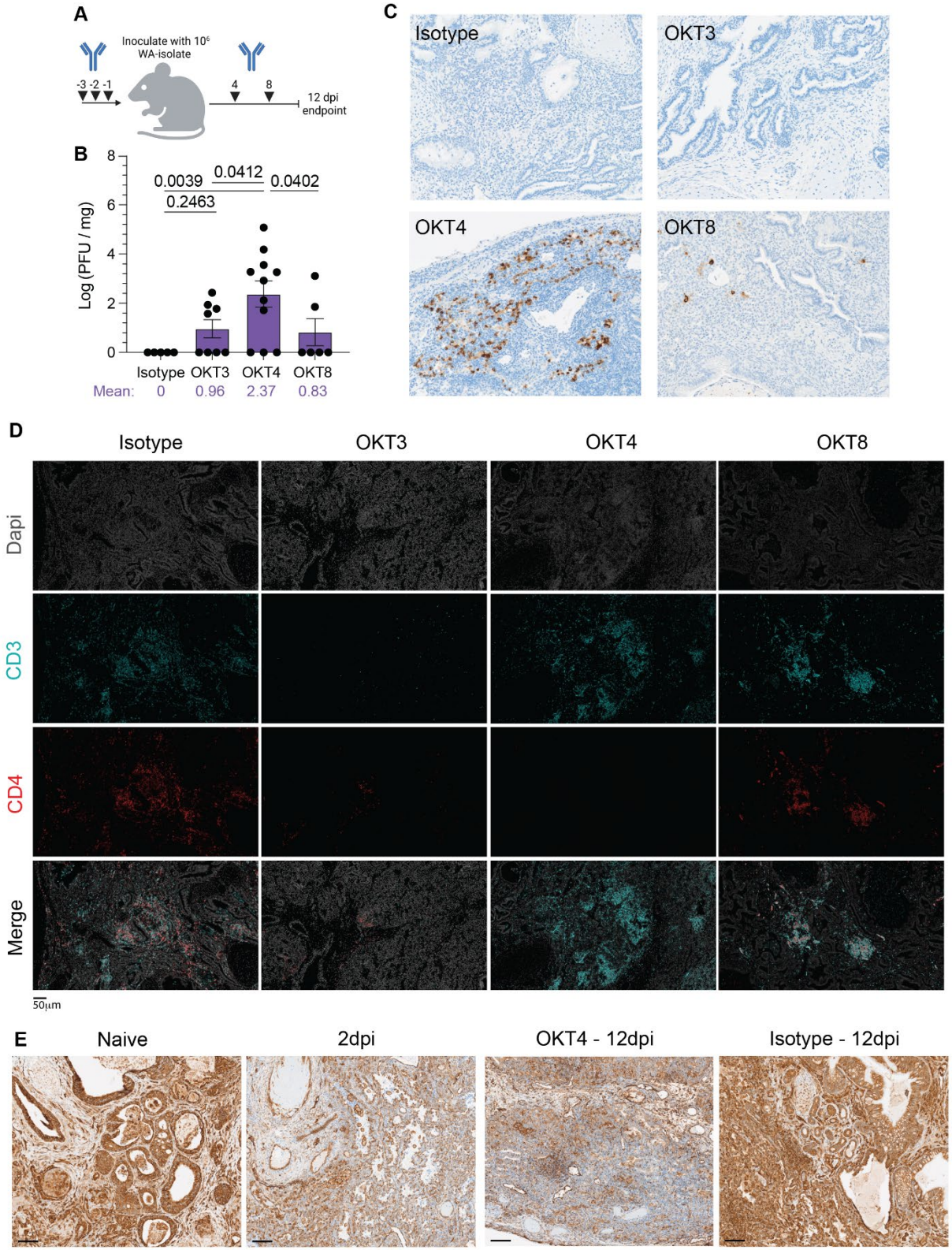
A
Inoculate with 10⁶ WA-isolate
-3 -2 -1
4 8
12 dpi endpoint
B
Log (PFU / mg)
0.0039
0.0412
0.0402
0.2463
Isotype OKT3 OKT4 OKT8
Mean: 0 0.96 2.37 0.83
C
Isotype
OKT3
OKT4
OKT8
D
Isotype
OKT3
OKT4
OKT8
Dapi
CD3
CD4
Merge
50µm
E
Naive
2dpi
OKT4 - 12dpi
Isotype - 12dpi

831

832 **Figure 2. Systemic depletion of CD4+ cells results in persistent infection of fLX. (A)** BLT-L
833 mice were administered 200 μg of anti-CD3e (OKT3), anti-CD4 (OKT4), anti-CD8 (OKT8) or
834 IgG2a isotype. **(B)** Viral titer (log(PFU/mg)) in fLX extracted from BLT-L mice treated with isotype,
835 OKT3, OKT4, or OKT8 antibody at 12 dpi. **(C)** Immunohistochemistry for SARS-CoV-2 N protein
836 on fLX of depleted or non-depleted BLT-L mice at 12 dpi. **(D)** Multiplex immunohistochemistry on
837 fLX of depleted or non-depleted BLT-L mice at 12 dpi. Dapi = gray, CD3 = teal, CD4 = red. Scale
838 bar = 50 μm. **(E)** MHC-I staining of fLX tissue sections (anti-MHC class I (EMR8-5) CST 88274)
839 extracted from naïve mice, OKT4-treated mice (12 dpi), or from infected fLX at 2 and 12 dpi. Scale
840 bar = 100 μM
841
842
843
844
845
846
847
848
849
850
851
852
853
854
855
856

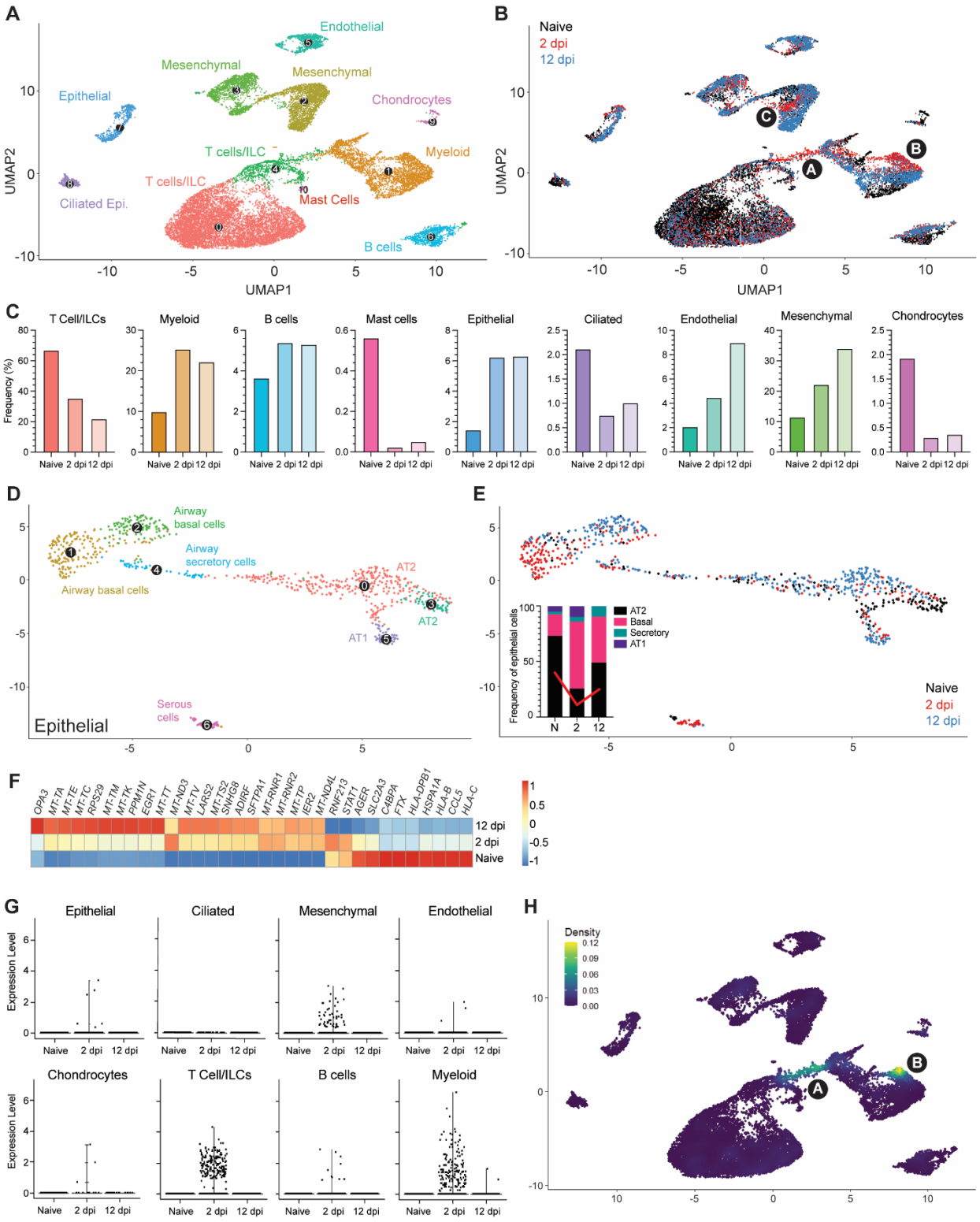
A
Endothelial
Mesenchymal
Mesenchymal
Epithelial
Chondrocytes
T cells/ILC
Myeloid
T cells/ILC
Mast Cells
Ciliated Epi.
B cells
UMAP2
UMAP1
B
Naive
2 dpi
12 dpi
C
T Cell/ILCs
Myeloid
B cells
Mast cells
Epithelial
Ciliated
Endothelial
Mesenchymal
Chondrocytes
Frequency (%)
Naive 2 dpi 12 dpi
D
Airway basal cells
Airway secretory cells
Airway basal cells
AT2
AT2
AT1
Serous cells
Epithelial
E
AT2
Basal
Secretory
AT1
Frequency of epithelial cells
N 2 12
Naive
2 dpi
12 dpi
F
OPA3 MT-TA MT-TE MT-TC RPS29 MT-TM MT-TK PPIMIN EGR1 MT-TT MT-ND3 MT-TV LARS2 MT-TS2 SNHG8 ADIRF SFTPA1 MT-RNR1 MT-RNR2 MT-TP IER2 MT-ND4L RNF213 STAT1 AGER SLC2A3 C4BPA FTX HLA-DPB1 HSPA1A HLA-B CCL5 HLA-C
12 dpi
2 dpi
Naive
G
Epithelial
Ciliated
Mesenchymal
Endothelial
Chondrocytes
T Cell/ILCs
B cells
Myeloid
Expression Level
Naive 2 dpi 12 dpi
H
Density
0.12
0.09
0.06
0.03
0.00

857

858

859

860 **Figure 3**. **Cellular remodeling and viral dynamics in fLX upon SARS-CoV-2 infection**

861 Single cell RNA sequencing analysis was performed on single cell suspensions of naïve fLX and
862 fLX at 2 and 12 dpi. Naïve n=3 fLX (9,605 cells), 2 dpi n=2 fLX (4,405 cells), and 12 dpi n = 2 fLX
863 (5,857 cells). **(A)** UMAP plot clustering of the human cell compartment of naïve fLX and fLX at 2
864 and 12 dpi. **(B)** Temporal annotation of the human clusters on the UMAP plot: naïve (black), 2 dpi
865 (red), 12 dpi (blue). Sub-clusters unique to 2 dpi are annotated by A (T cell compartment), B
866 (myeloid compartment) and C (mesenchymal compartment). **(C)** Frequency of each cell
867 compartment determined by single cell RNA-sequencing. **(D)** Dot plots displaying the expression
868 of SARS-CoV-2 viral RNA transcripts identified in scRNA-seq. **(E)** UMAP plot showing the
869 distribution of SARS-CoV-2 viral RNA transcripts across all human cell clusters and time points.
870 **(F)** UMAP plot sub-clustering of the human AT2 compartment in fLX across all time points. **(G)**
871 Temporal annotation of the human epithelial sub-clusters on the UMAP plot: naïve (black), 2 dpi
872 (red), 12 dpi (blue). The inset graph indicates the change in frequency of each compartment (AT2;
873 black, Basal; pink, Secretory; teal, and AT1; purple) within the epithelial compartment. Red line
874 indicates the change in the AT2 compartment over time. **(H)** Heatmap displaying the relative
875 expression (from -1 to 1) of the top differentially regulated genes over the course of infection within
876 the AT2 compartment.

877

878

879

880

881

882

883

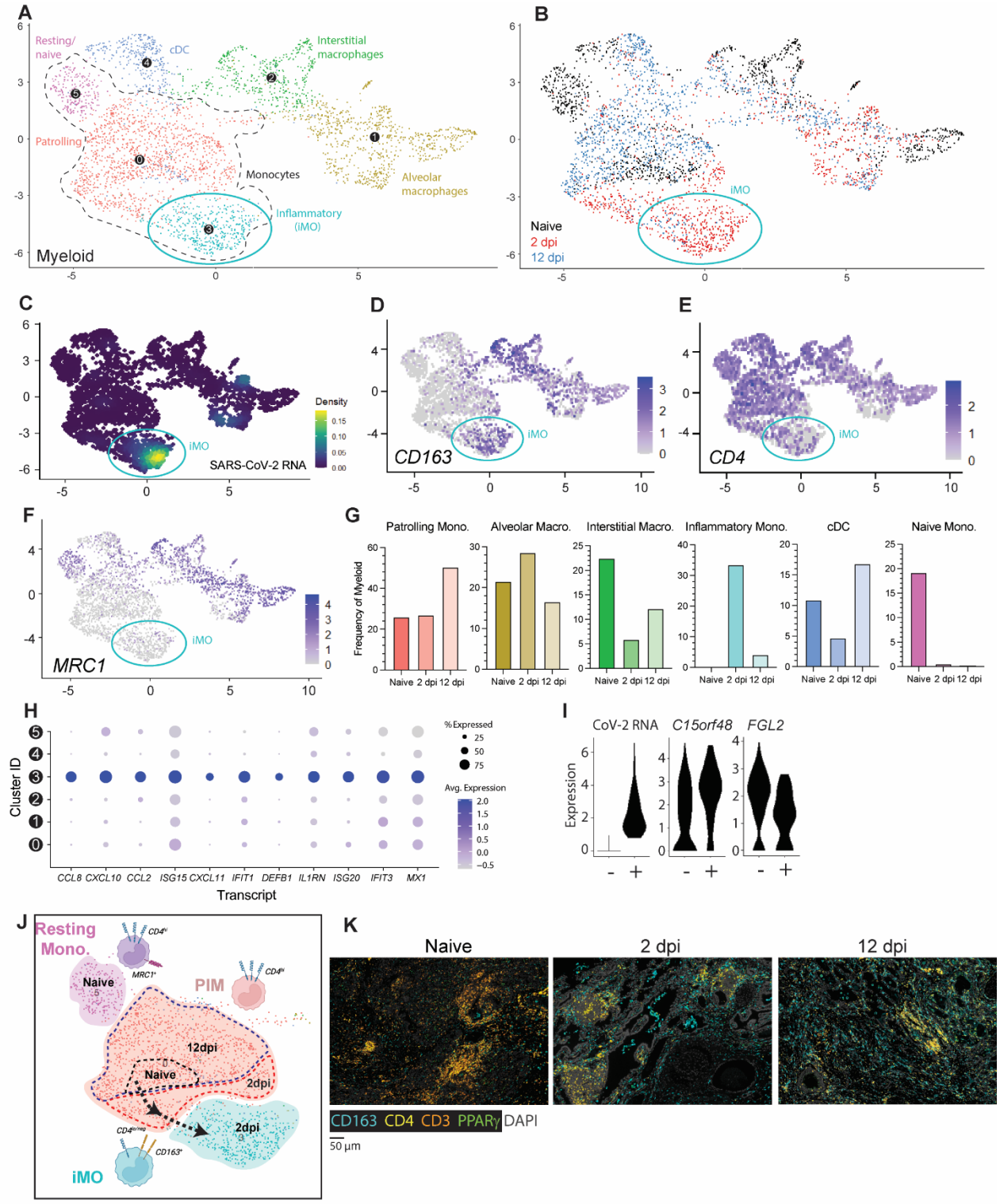
A
Resting/ naive
cDC
Interstitial macrophages
Patrolling
Monocytes
Alveolar macrophages
Inflammatory (iMO)
Myeloid
B
iMO
Naive
2 dpi
12 dpi
C
iMO
SARS-CoV-2 RNA
Density
D
iMO
CD163
E
iMO
CD4
F
iMO
MRC1
G
Patrolling Mono.
Alveolar Macro.
Interstitial Macro.
Inflammatory Mono.
cDC
Naive Mono.
Frequency of Myeloid
Naive 2 dpi 12 dpi
H
Cluster ID
% Expressed
Avg. Expression
CCL8 CXCL10 CCL2 ISG15 CXCL11 IFIT1 DEFB1 IL1RN ISG20 IFIT3 MX1
Transcript
I
CoV-2 RNA
C15orf48
FGL2
Expression
J
Resting Mono.
Naive
PIM
12dpi
Naive
2dpi
2dpi
iMO
K
Naive
2 dpi
12 dpi
CD163 CD4 CD3 PPARγ DAPI
50 µm

884

885

886 **Figure 4. CD163+ extravascular inflammatory monocytes arise during acute viral infection**
887 **and are predominant antiviral mediators. (A)** UMAP plot showing sub-clustering of the human
888 myeloid compartment of fLX across all time points. **(B)** Temporal annotation of the myeloid sub-
889 clusters on the UMAP plot: naïve (black), 2 dpi (red), 12 dpi (blue). ExiMO sub-cluster is indicated
890 with a blue circle. **(C)** UMAP plot (all time points) showing the distribution of SARS-CoV-2 viral
891 RNA transcripts in the myeloid compartment. **(D-F)** UMAP plot showing the expression of CD*163*
892 **(D),** *CD4* **(E)**, and *MRC1* **(F)** across myeloid sub-sets. **(G)** Frequency of each myeloid sub-cluster
893 by timepoint. **(H)** Relative expression of highly upregulated ISGs and inflammatory markers in
894 each of the myeloid sub-clusters. **(I)** Violin plots showing expression level of differentially
895 expressed genes between SARS-CoV-2 positive and negative ExiMO (sub-cluster 3). **(J)**
896 Schematic representation of proposed temporal myeloid dynamics during infection. Black arrows
897 represent differentiation dynamics during infection. **(K)** Multiplex fluorescent
898 immunohistochemistry of naïve fLX and fLX at 2 and 12 dpi. CD163: teal, CD4: yellow, CD3:
899 orange, PPARγ: green, Dapi: gray. Two representative images. Scale bar = 100 μM.
900
901
902
903
904
905
906
907
908
909

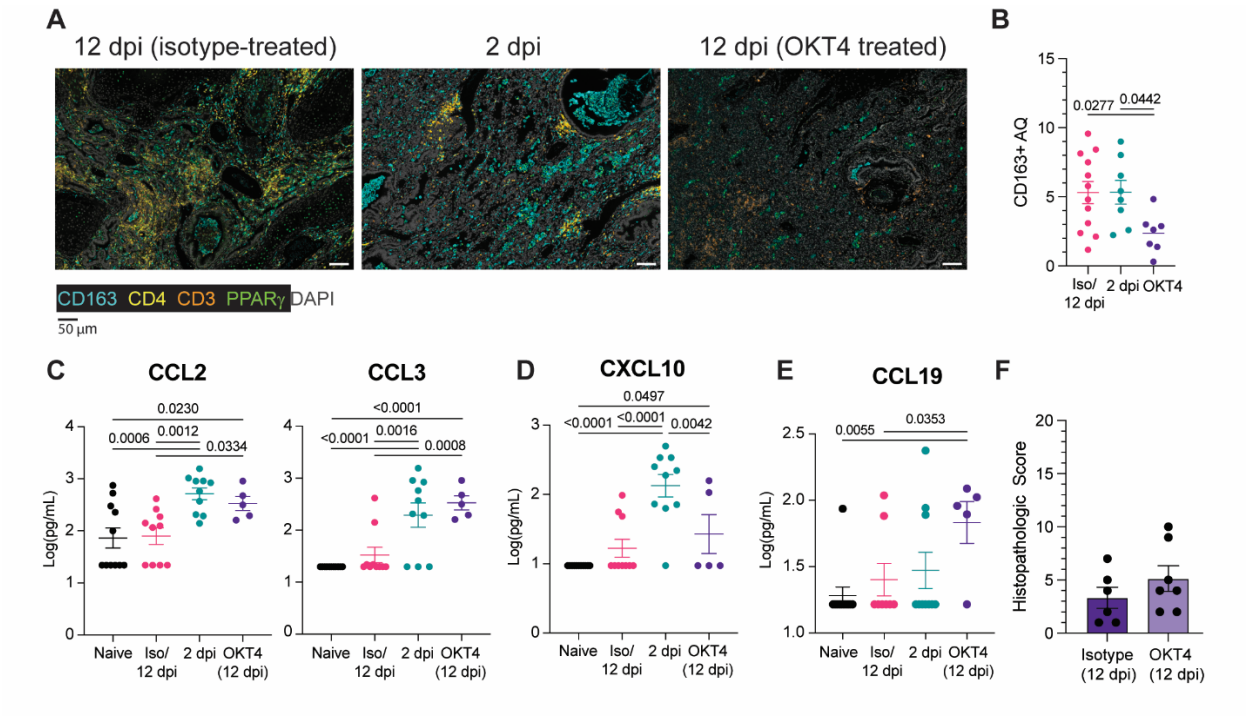

910

911 **Figure 5. CD4+ cell depletion reduces CD163+ recruitment in fLX, promotes immune**
912 **tolerance and results in signatures of chronic infection. (A-B)** Multiplex fluorescent
913 immunohistochemistry (A) and CD163+ area quantification (AQ) (B) of fLX that resolved infection
914 (12 dpi, isotype treated), or eliciting acute (2 dpi) or persistent infection (12 dpi, OKT4 treated).
915 CD163: teal, CD4: yellow, CD3: orange, PPARγ: green, Dapi: gray. Scale bar = 50 µM. **(C-E)**
916 Cytokine quantification (C: CCL2/3, D: CXCL10, E: CCL19) in the serum of naïve, infected (2 dpi
917 and 12 dpi isotype-treated or not) and OKT4-treated BLT-L mice (12 dpi). **(F)** Histopathological
918 scoring of fLX extracted from isotype and OKT4-depleted BLT-L mice (12 dpi). Error bars indicate
919 mean ± Standard error of the mean. One-*way ANOVA, t-test. p-values are indicated on graphs.*

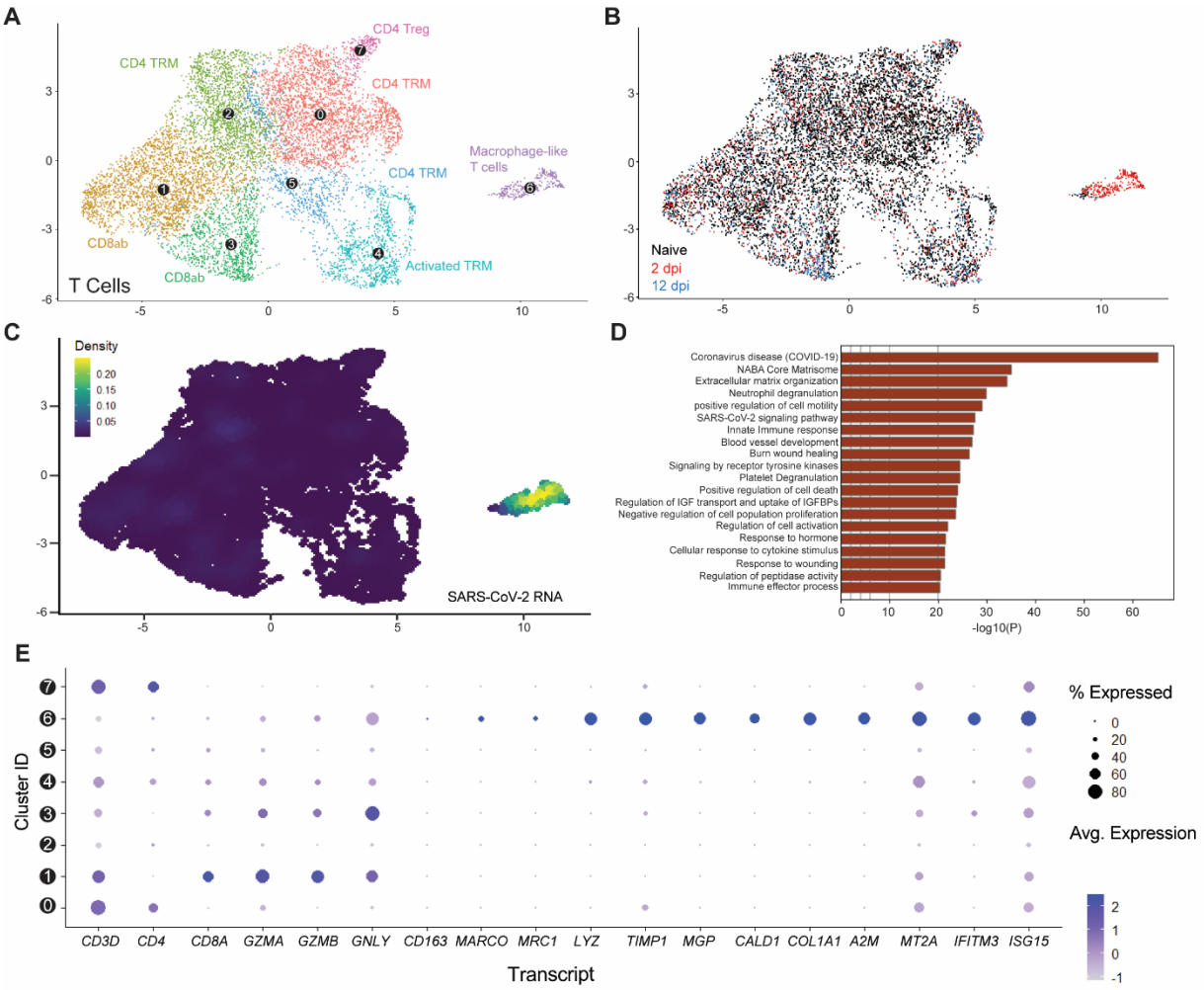

Figure 6. Macrophage-like T-cell emerges upon acute infection and are enriched in viral RNA. (A) UMAP plot showing the sub-clustering of the human T-cell compartment of fLX across all time points. **(B)** Temporal annotation of the human T-cell sub-clusters on the UMAP plot: naïve (black), 2 dpi (red), 12 dpi (blue). **(C)** UMAP plot (all time points) showing the distribution of SARS-CoV-2 viral RNA transcripts in the T-cell compartment. **(D)** Go-term analysis showing the most highly upregulated signaling pathways in the macrophage-like T-cell sub-cluster (sub-cluster 6). **(E)** Relative expression of T-cells, macrophage, mesenchymal and antiviral markers within each of the T-cell sub-clusters (From 0 to 7; as labeled in panel A.).

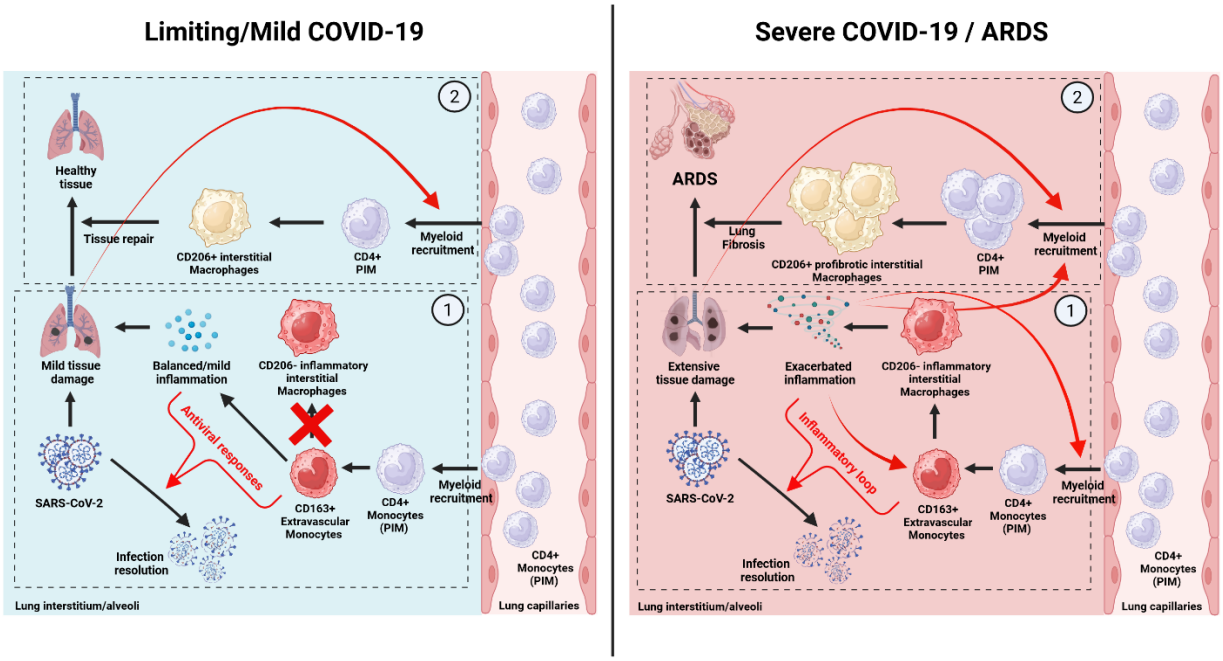

Figure 7. The inflammatory fate of ExiMO may define the clinical course of SARS-CoV-2 infection. During mild COVID-19 disease (left window), robust ExiMO antiviral responses and phagocytosis drive infection resolution in the absence of differentiation into CD206- inflammatory interstitial macrophages (1). Mild tissue damage caused by virally-induced cytopathic effects and moderate inflammation drive the recruitment of CD206+ interstitial macrophages, which promote tissue repair (2). During severe COVID-19 disease (right window), ExiMO differentiate into CD206- inflammatory interstitial macrophages. Antiviral responses and inflammation are exacerbated, triggering an inflammatory positive-feedback loop resolving infection at the expense of severe tissue damage (1). Such damages promote the extensive recruitment of CD206+ interstitial macrophages with pro-fibrotic functions, favoring the development of lung fibrosis and increasing the incidence of ARDS (2).

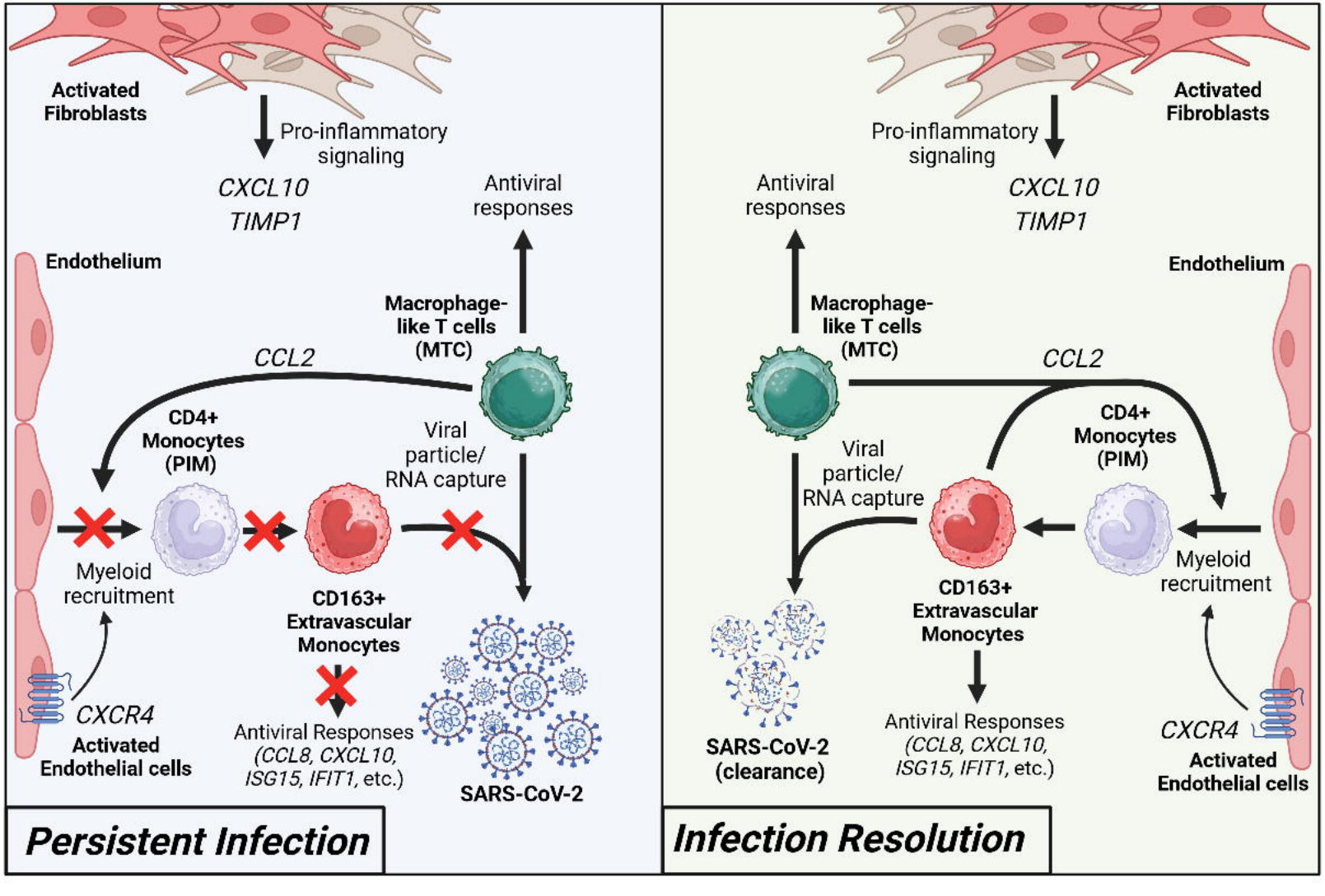
Activated Fibroblasts
Pro-inflammatory signaling
CXCL10
TIMP1
Antiviral responses
Endothelium
Macrophage-like T cells (MTC)
CCL2
CD4+ Monocytes (PIM)
Viral particle/ RNA capture
Myeloid recruitment
CD163+ Extravascular Monocytes
CXCR4
Activated Endothelial cells
Antiviral Responses (CCL8, CXCL10, ISG15, IFIT1, etc.)
SARS-CoV-2
Persistent Infection
Activated Fibroblasts
Pro-inflammatory signaling
CXCL10
TIMP1
Antiviral responses
Endothelium
Macrophage-like T cells (MTC)
CCL2
CD4+ Monocytes (PIM)
Viral particle/ RNA capture
Myeloid recruitment
CD163+ Extravascular Monocytes
SARS-CoV-2 (clearance)
Antiviral Responses (CCL8, CXCL10, ISG15, IFIT1, etc.)
CXCR4
Activated Endothelial cells
Infection Resolution